Volume 4 Issue 1

MERSIN PHOTOGRAMMETRY JOURNAL

The MERSİN PHOTOGRAMMETRY JOURNAL (MEPHOJ)

THE MERSİN PHOTOGRAMMETRY JOURNAL (MEPHOJ) publishes original and innovative contributions in photogrammetric applications ranging from the integration of instruments, methodologies, and technologies and their respective uses in the environmental sciences, engineering, and other natural sciences. Mersin Photogrammerty Journal is a branch of science that widely applied in many scientific disciplines. MEPHOJ aims to cover the entirety of Photogrammetry and Photogrammetric aplications about Geosciences, including their application domains. MEPHOJ strives to encourage scientists to publish experimental, theoretical, and computational results as detailed as possible so that results can be easily reproduced.

MEPHOJ is a double peer-reviewed (blind) OPEN ACCESS JOURNAL that publishes professional level research articles and subject reviews exclusively in English. It allows authors to submit articles online and track his or her progress via its web interface. All manuscripts will undergo a refereeing process; acceptance for publication is based on at least two positive reviews. The journal publishes research and review papers, professional communication, and technical notes. MEPHOJ does not charge for any article submissions or for processing.

CORRESPONDENCE ADDRESS
Journal Contact: myakar@mersin.edu.tr

CONTENTS

Volume 4 - Issue 1

RESEARCH ARTICLES

Mersin Photogrammetry Journal

https://dergipark.org.tr/en/pub/mephoj

e-ISSN 2687-654X

Orthophoto production and accuracy analysis with UAV photogrammetry

Ramazan Güngör*[1], Melis Uzar [2], Bilal Atak [3], Osman Salih Yılmaz [1], Erdal Gümüş [4]

[1]*Manisa Celal Bayar University, Demirci Vocational School, Department of Urban Planning, Manisa, Türkiye*
[2]*Yıldız Technical University, Geomatics Engineering Department, Türkiye*
[3]*Kırşehir Ahi Evran University, Kaman Vocational School, Department of Urban Planning, Kırşehir, Türkiye*
[4]*Balıkesir University, Geography Department, Balıkesir, Türkiye*

Keywords
Spatial accuracy
UAV
Photogrammetry
Orthophoto Production
DTM

ResearchArticle
DOI:10.53093/mephoj.1122615

Received: 28.05.2022
Accepted: 02.07.2022

Abstract

Undoubtedly, Unmanned Aerial Vehicles (UAVs) are one of today's most functional technology products. In recent years, UAVs integrated with different sensors and transformed into harmony with advanced technology are developing rapidly and used in various applications to obtain spatial data. With UAV photogrammetry, images of target areas can be obtained quickly, at low cost, with high accuracy, and up to date. In addition to the advantages and success of existing methods for orthophoto production in large areas with classical photogrammetry, it is observed that the accuracy of these methods decreases in detecting changes in geometric properties, especially in small-scale areas. For this reason, obtaining geometric accuracy with the desired precision, which is of great importance in orthophoto production with UAV photogrammetry, has made it the basis for preference over classical methods. In this study, autonomous flights were carried out with DJI Mavic-2 Pro UAV in the selected pilot region, and orthophoto, Digital Elevation Model (DEM), and Digital Terrain Model (DTM) were produced as a result of processing the images obtained. To determine the geometric accuracy of the orthophoto, its coordinates were measured by the CORS-GPS method, and ten ground control points (GCP) were used. As a result of the accuracy analysis of the produced orthophoto, the spatial accuracy in the easting (ΔE) direction is ±6.9 cm, the spatial accuracy in the northing (ΔN) direction is ±7.8 cm, and the spatial accuracy in the height (ΔH) direction is ±10.3 cm.

1. Introduction

The map production is usually a time-consuming process depending on the project's purpose, scale, and accuracy. However, with the advances in technology in recent years, unmanned aerial vehicles (UAVs) have been used in the field of remote sensing (RS) and photogrammetry, which produce high- accuracy data and produce high-accuracy results in a short time [1, 2]. The UAV history dates back to 1850 and was first used for military purposes [3]. Later, aerial vehicles were developed for photogrammetric purposes and were integrated into this field, and thus the name "UAV Photogrammetry" took its place in the literature. UAV photogrammetry describes a photogrammetric measurement platform that works remotely, semi-autonomously, or autonomously with a digital camera [4]. The camera carried by UAVs provide high-resolution aerial photographs at a low cost way in cloudy weather where the ground view is not clear [5]. In addition to optical cameras, thermal or infrared, multispectral, hyperspectral, and Light Detection and Ranging (LiDAR) sensors can be mounted on UAVs to increase their data collection capabilities [6]. In this way, it is possible to detect wideband ranges within the electromagnetic spectrum [7]. To ensure spatial accuracy and precision, which is an important issue, especially in cartography activities, the Global Navigation Satellite Systems (GNSS) may also be included in its structure[8]. In this way, a fully-integrated UAVs have been created [9]. The use of UAVs in photogrammetry studies, whose hardware and software are developed day by day, has become widespread, and UAV technology has allowed the acquisition of overlay photographs suitable for photogrammetric purposes [10].

* **Corresponding Author**

*(ramazan.gungor@cbu.edu.tr) ORCID ID 0000-0002-6338-8554
(auzar@yildiz.edu.tr) ORCID ID 0000-0003-0873-3797
(bilal.atak@ahievran.edu.tr) ORCID ID 0000-0002-1460-0707
(osmansalih.yilmaz@cbu.edu.tr) ORCID ID 0000-0003-4632-9349
(erdalgumus@hotmail.com) ORCID ID 0000-0003-0815-340X

Cite this article

Güngör, R., Uzar, M., Atak, B., Yılmaz, O. S., & Gümüş, E. (2022). Orthophoto production and accuracy analysis with UAV photogrammetry. *Mersin Photogrammetry Journal, 4(1), 01-06*

Today, aerial photographs obtained with this application method are evaluated with photogrammetric compilation processes and final products such as digital elevation model (DEM), digital terrain model (DTM), and orthophoto are obtained [11]. An orthophoto is an image which has vertical projection position through differential correction or ortho-rectification [12]. In other words, they are images with a fixed scale at each point and show the current state of the terrain by eliminating errors caused by obliquity and rotation effects and topographical height differences that occur in aerial photographs[13]. Orthophotos, which express the current situation of the land are obtained by associating satellite images or aerial photos of an area with DEM [14]. Unlike aerial photographs, since they have a high spatial resolution, angle, distance, and size measurements can be made [15].

Orthophoto production of an area requires many steps such as pre-flight planning, data acquisition, calibration and image processing. During the application of each step, different types of errors will appear on the orthophotos and these errors affect the final product [16]. Therefore, accuracy should be evaluated for digital orthophotos. In this evaluation phase, different parameters are used, and the overall accuracy is determined according to the values on these parameters. Numerous studies have been conducted on the production of orthophoto maps obtained by UAVs, and it has been determined that UAVs ensure international spatial quality standards [17–20]. However, ground control points (GCP) are established on the land to detect the spatial errors during orthophoto production. These points are measured with Real-Time Kinematic (RTK) measurements or Continuously Operating Reference Stations (CORS) system working in TUSAGA-Active System to be used as exterior orientation parameters [21]. 3D accuracies of digital orthophoto images and the methods used are shown in the "Accuracy Standards for Digital Geospatial Data March 2014" directive implemented to affect the American Society for Photogrammetry and Remote Sensing (ASPRS)[22].

This study aims to analyze the accuracy of the products produced by UAV photogrammetry. Within the scope of the survey, orthophoto, DEM, and DTM of the selected pilot region were delivered. In addition, the location data to determine the accuracies were obtained with the GPS/GNSS receiver, and the results were compared and analyzed.

2. Material

To investigate the spatial accuracy of the produced orthophotos, 10 GCPs were installed in the study area, and the coordinate values were measured with the GPS/GNSS technique. Then the orthophoto production stage is started. In this section, grids whose midpoint coordinates are defined in the field coordinate system are defined. Then, the midpoint coordinates of the pixels in these grids are taken from the DEM, and the interior and exterior orientation parameters are calculated from image coordinates. Afterward, interpolation is made by calculating pixel coordinate values from image coordinates (Fig. 1).

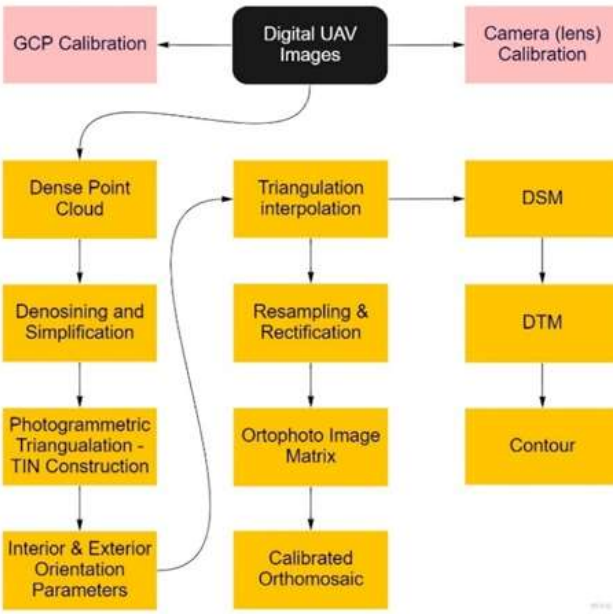

Figure 1. The flow chart of the methodology

2.1. Study Area

Within the scope of the study, Ida Madra Geopark, Sindirgi district Zindankayasi Archaeological site (Phrygian altar) (Fig. 2) was chosen as the test area to produce orthophoto images, analyze their accuracy and compare the resulting surface models.

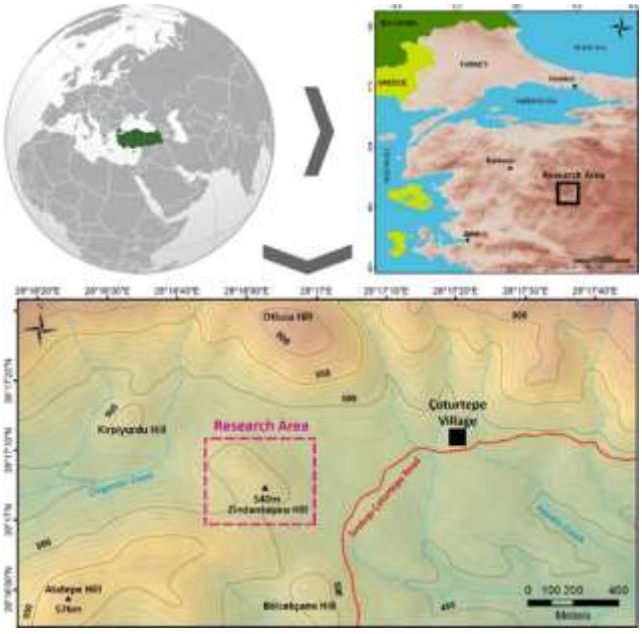

Figure 2. Study area

2.2. Data Acquisition

Within the scope of the study, the horizontal (Northing, Easting) and vertical (Ellipsoidal height) coordinate information of the GCP to be used for location accuracy were measured with the FOIF A90 geodetic GNSS receiver connected to the TUSAGA-Active system. The measurement process was carried out as a total of 50 epochs. In addition, 10 control points (CP) were measured over the land to examine the 3D accuracies of orthophoto maps. The image of GCP and CP points are given in Figure 3.

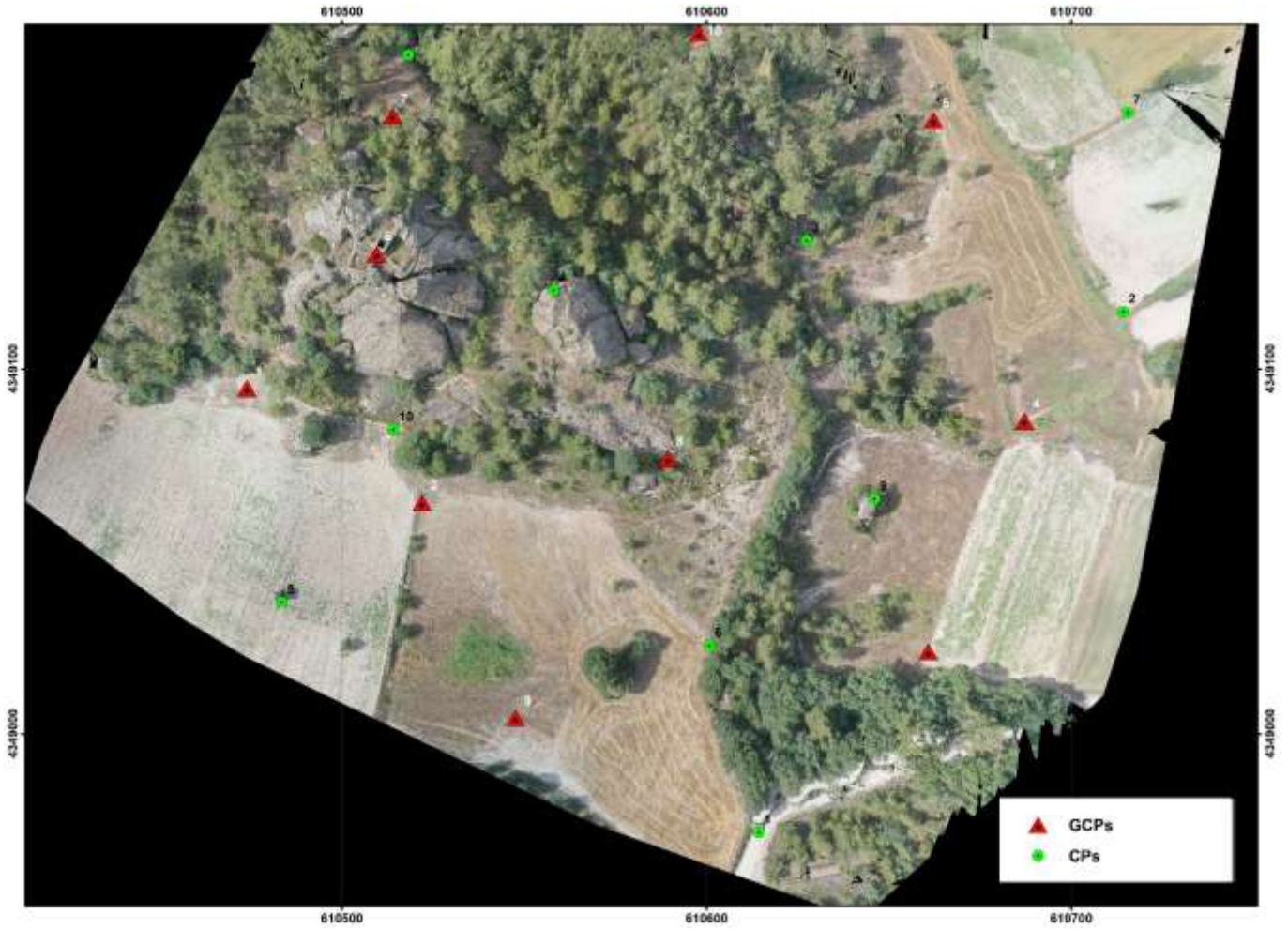

Figure 3. GCP and CP points

After the necessary spatial measurements were made for accuracy assessment, flight planning was carried out to produce high-resolution orthophotos, DEMs, and DTMs of the study area with the UAV. In this planning, in addition to the take-off and landing information of the UAV, data such as flight altitude, overlay ratios of the images obtained, resolution information, and image acquisition angle are included. A view from the flight plan and management screen is shown in Figure 4.

Figure 4. The flight plan and management screen

After the planning stage, autonomous flights were made with the DJI Mavic 2 Pro UAV with Hasselblad 20MP/UHD 4K Gimbal camera features. The flight process was carried out for approximately 25 minutes, at 50 m from the ground, with a longitudinal overlap rate of 80% and a transverse overlap rate of 70%. In addition, a total of 126 images of the study area with a resolution of 159x255 m were obtained at 1.25 cm/px ground sampling distance (GSD), and the field study was completed.

2.3. Assessment of Data

After the flight process, the data produced by the UAV and GPS were transferred to the workstation for photogrammetric compilation and orthophoto production. In the application, photogrammetric compilation processes were made with Pix4D Mapper. The Structure From Motion (SFM) method is widely used to assess the data obtained using UAVs for photogrammetric purposes. Unlike conventional photogrammetry, this method does not need interior orientation parameters. Instead, it calculates the camera calibration and orientation parameters using enough GCP [10]. In addition, it performs scene modeling with bundle adjustment by mapping details on multiple images taken with specific ratios of overlap [23–25]. Earth science, especially in recent years [26, 27], geomorphology analysis [28], agriculture [29], and archaeology [30], the SFM technique is widely used in applications such as high-resolution images that allow you to work on a low-cost, and easy-to-use is the application of photogrammetry [31, 32].

3. Method

3.1. Accuracy Assessment

Different methods are used to assess the accuracy of the products obtained by photogrammetric methods. In studies conducted for this purpose, techniques such as Proportional Error, Root Mean Square Error (RMSE), and Probabilistic Error are generally used [5, 6].

3.1.1. Root Mean Square Error

In this study, the RMSE method was used for accuracy assessment. This method is described as the square root of the mean of the difference in orthophoto or DEM coordinates produced with the measured reference GCP and CP coordinates [33]. First, calculate the RMSE in the northing (N) direction ($RMSE_N$) in equation 1, the RMSE in the easting (E) direction ($RMSE_E$) in equation 2, the RMSE in the height (H) ($RMSE_H$) in equation 3 and the horizontal spatial error ($RMSE_{NE}$) The mathematical expression used for this is shown in equation 4.

$$RMSE_N=\sqrt{\frac{\sum \Delta N^2}{n}} \quad (1)$$

$$RMSE_E=\sqrt{\frac{\sum \Delta E^2}{n}} \quad (2)$$

$$RMSE_H=\sqrt{\frac{\sum \Delta H^2}{n}} \quad (3)$$

$$RMSE_{NE}=\sqrt{RMSEN^2 + RMSEE^2} \quad (4)$$

where ΔN is the difference between the northing coordinates, ΔE is the difference between the easting coordinates, and n is the number of points.

4. Results

As a result of the assessment of the data obtained, 126 high-resolution aerial photographs of the study area obtained by the autonomous flights of the UAV were used, using an orthophoto with a spatial resolution of 1.74 cm (Figure 5), a DEM with a spatial resolution of 8.67 cm (Figure 6) and a 1.74 cm (Fig. 7) was produced at cm spatial resolution. ArcMap 10.4 software was used for the accuracy assessment of the produced orthophoto. In addition, the coordinate values obtained from the images and models were compared on horizontal and vertical surfaces using the GCP and CP coordinate values measured with the GPS/GNSS receiver.

Within the scope of the study, the results of the products produced by the UAV photogrammetry method were compared with the results obtained using satellite-based measurement techniques, and an accuracy assessment was made. The spatial information received over the orthophoto and measured by the GPS/GNSS receiver is shown in Table 1, with the differences occurring at each point. Using these calculated differences, $RMSE_E$= ±6.9 cm and $RMSE_N$= ±7.8 cm in the horizontal direction were determined. Therefore, the horizontal spatial error is $RMSE_{NE}$=10.4 cm. In addition, the DEM produced as a result of the topographic data acquisition process and the DEM produced by the UAV were compared, and the vertical direction was determined as $RMSE_H$ = ±10.3 cm at the same reference points.

A DEM of the study area was produced using the height values obtained by topographic acquisition with the GPS/GNSS receiver, and this model was compared with the DEM produced by the UAV. The comparison was made over the pixel values with the exact location on both DEMs. In the comparison process made by taking the pixel differences, the two height models determined differences between -14 cm and +24 cm.

Figure 5. Orthophoto produced by UAV

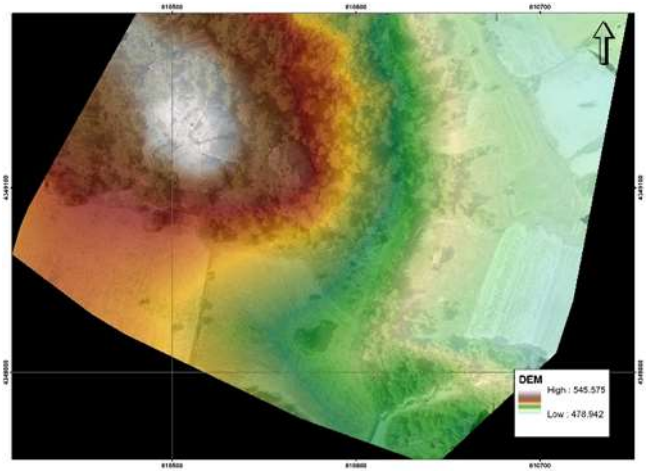

Figure 6. DEM produced by UAV

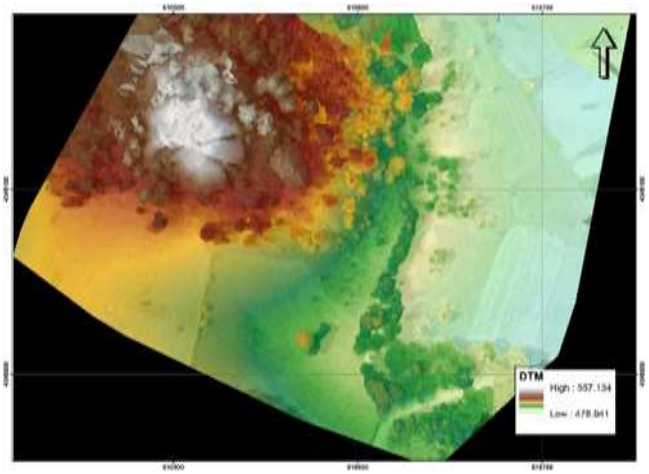

Figure 7. DTM produced by UAV

Table 1. Position information and coordinate differences of the points used for control purposes

Orthophoto (m)				GPS/CORS (m)			Difference (m)= Orthophoto(m)-GPS/CORS(m)		
Point Name	**Northing (N)**	**Easting (E)**	**Height (H)**	**Northing (N)**	**Easting (E)**	**Elliosoidal Height (H)**	**Δ(N)**	**Δ(E)**	**Δ(H)**
GCP 1	4349094.753	610473.944	516.21	4349094.806	610473.884	516.29	-0.053	0.060	-0.080
GCP 2	4349063.439	610521.964	507.83	4349063.525	610522.061	507.70	-0.086	-0.096	0.129
GCP 3	4349022.589	610660.717	483.02	4349022.579	610660.705	483.04	0.010	0.012	-0.015
GCP 4	4349085.814	610687.080	483.75	4349085.852	610687.038	483.81	-0.037	0.042	-0.056
GCP 5	4349168.259	610662.209	484.75	4349168.235	610662.236	484.72	0.024	-0.027	0.036
GCP 6	4349131.640	610509.544	545.15	4349131.663	610509.518	545.18	-0.023	0.026	-0.034
GCP 7	4349169.478	610513.836	533.28	4349169.617	610513.991	533.07	-0.138	-0.156	0.207
GCP 8	4349075.440	610589.323	502.65	4349075.531	610589.425	502.52	-0.091	-0.102	0.136
GCP 9	4349004.362	610547.608	500.16	4349004.379	610547.589	500.13	-0.017	0.019	0.026
GCP10	4349192.111	610597.773	500.92	4349192.114	610597.769	500.92	-0.003	0.004	-0.005
CP1	4348973.053	610614.265	495.73	4348973.033	610614.243	495.76	0.020	0.023	-0.030
CP2	4349115.717	610714.172	481.75	4349115.722	610714.178	481.74	-0.005	-0.006	0.008
CP3	4349135.190	610627.389	494.56	4349135.197	610627.396	494.55	-0.007	-0.007	0.010
CP4	4349121.643	610557.962	524.24	4349121.484	610558.141	524.00	0.159	-0.179	0.239
CP5	4349036.130	610483.455	507.47	4349036.108	610483.480	507.50	0.022	-0.025	-0.033
CP6	4349024.277	610600.719	493.04	4349024.379	610600.834	492.88	-0.103	-0.115	0.154
CP7	4349170.327	610715.442	480.29	4349170.423	610715.335	480.43	-0.096	0.108	-0.144
CP8	4349186.089	610518.126	523.20	4349186.098	610518.136	523.18	-0.009	-0.010	0.013
CP9	4349064.380	610645.973	488.30	4349064.367	610645.958	488.32	0.014	0.015	-0.021
CP10	4349083.430	610514.105	513.39	4349083.365	610514.178	513.30	0.066	-0.074	0.098

5. Conclusion

In the study, the UAV photogrammetry method was utilized as an alternative to classical aerial photogrammetry, and the spatial accuracy of the obtained products was examined. As a result, the horizontal spatial accuracy of the orthophotos produced within the scope of the study was determined as ±10.4 cm and the vertical spatial accuracy as ±10.3 cm. According to these results, it was concluded that the UAV photogrammetry method could be used to produce maps at different scales. In addition, when DEMs produced by the UAV photogrammetry method and DEMs created using satellite and space techniques are compared, their spatial accuracy has shown that they can be alternative methods to each other.

The UAV photogrammetry can model and map archaeological details to record cultural heritage. In studies where precise modeling will be carried out, higher accuracy data acquisition can be achieved by mounting a lidar system on the UAVs.

Acknowledgement

Acknowledgements of support for the project/paper/author are welcome.

Author contributions

Ramazan Güngör: Conceptualization, Methodology, Writing-Original draft preparation, Software, Validation, Visualization, Investigation, **Melis Uzar**: Methodology, Writing-Reviewing and Editing, **Bilal Atak**: Data curation, Writing-Original draft preparation, **Osman Salih Yılmaz**: Writing-Reviewing and Editing, **Erdal Gümüş**: Data curation, Software and Editing.

Conflicts of interest

The authors declare no conflicts of interest.

References

1. Yılmaz, H. M., & Yakar, M. (2008). Computing of volume of excavation areas by digital close range photogrammetry.
2. Yakar, M., Yılmaz, H. M., & Mutluoğlu, H. M. (2009). Hacim Hesaplamalarında Laser Tarama ve Yersel Fotogrametrinin Kullanılması, TMMOB Harita ve Kadastro Mühendisleri Odası 12. *Türkiye Harita Bilimsel ve Teknik Kurultayı, Ankara*.
3. Prisacariu, V. (2017). The history and the evolution of UAVs from the beginning till the 70s. *Journal of Defense Resources Management (JoDRM)*, *8*(1), 181-189.
4. Eisenbeiss, H. (2008, February). UAV photogrammetry in plant sciences and geology. In *6th ARIDA Workshop on" Innovations in 3D Measurement, Modeling and Visualization, Povo (Trento), Italy*.
5. Selek, E. *İHA ile üretilmiş ortofoto, sayısal arazi ve yüzey modeli performanslarının incelenmesi: Bursa ili örneği* (Master's thesis, Fen Bilimleri Enstitüsü).
6. Şener, E. (2019). İnsansız hava araçları kullanılarak Süleyman Demirel Üniversitesi yerleşkesinin yüksek çözünürlüklü ortofoto haritasının hazırlanması. *Mühendislik Bilimleri ve Tasarım Dergisi*, *7*(2), 393-402.

7. Yılmaz, H. M., Mutluoğlu, Ö., Ulvi, A., Yaman, A., & Bilgilioğlu, S. S. (2018). İnsansız hava aracı ile ortofoto üretimi ve Aksaray Üniversitesi kampüsü örneği. *Geomatik*, *3*(2), 129-136.
8. Alptekin, A., & Yakar, M. (2020). Determination of pond volume with using an unmanned aerial vehicle. *Mersin Photogrammetry Journal*, *2*(2), 59-63.
9. Gültekin, Y., Özemir, I., Uzar, M., & Şimşek, M. (2016). İnsansız hava aracları ile ortofoto ve sym üretimi. *Uzaktan algılama CBS Sempozyumu (UZAL-CBS 2016)*, 310-318.
10. Bakirman, T., Bayram, B., Akpinar, B., Karabulut, M. F., Bayrak, O. C., Yigitoglu, A., & Seker, D. Z. (2020). Implementation of ultra-light UAV systems for cultural heritage documentation. *Journal of Cultural Heritage*, *44*, 174-184.
11. Eisenbeiß, H. (2009). UAV photogrammetry.
12. Wolf, P. R., Dewitt, B. A., & Wilkinson, B. E. (2014). *Elements of Photogrammetry with Applications in GIS*. McGraw-Hill Education.
13. Özbalmumcu, M. (2007). Fotogrametrik Yöntemle Ortofoto Harita Üretiminin Temel Esasları, Ortofotonun Yararları ve Kullanım Alanları. *TUFUAB IX. Teknik Sempozyumu, İstanbul*.
14. Yılmaz, V., Akar, A., Akar, Ö., Güngör, O., Karslı, F., & Gökalp, E. (2013). İnsansiz hava araci ile üretilen ortofoto haritalarda doğruluk analizi. *Türkiye Ulusal Fotogrametri ve Uzaktan Algılama Birliği VII. Teknik Sempozyumu (TUFUAB'2013), 23-25 Mayıs 2013*.
15. Simard, P. G. (1997). *Accuracy of digital orthophotos* (Doctoral dissertation, University of New Brunswick).
16. Arslan, O., & YAĞCIOĞLU, K. Fotogrametrik nirengiyle üretilen ortofoto haritalar ile koordinat altyapısındaki değişimlerin analizi: İzmit Körfezi örneği. *Türkiye Fotogrametri Dergisi*, *3*(2), 37-45.
17. Arslan, O., & Yılmaz, P. (2020). Evaluating the Geometric Accuracy of Large Scale Digital Orthophotos Produced from Aerial Photography. *International Journal of Environment and Geoinformatics*, *7*(3), 265-271.
18. Dalamagkidis, K., Valavanis, K. P., & Piegl, L. A. (2008). Current status and future perspectives for unmanned aircraft system operations in the US. *Journal of Intelligent and Robotic Systems*, *52*(2), 313-329.
19. Mesas-Carrascosa, F. J., Rumbao, I. C., Berrocal, J. A. B., & Porras, A. G. F. (2014). Positional quality assessment of orthophotos obtained from sensors onboard multi-rotor UAV platforms. *Sensors*, *14*(12), 22394-22407.
20. Sai, S. S., Tjahjadi, M. E., & Rokhmana, C. A. (2019). Geometric accuracy assessments of orthophoto production from uav aerial images. *KnE Engineering*, 333-344.
21. Akar., A., Akar, Ö., & Bayata, H. F. (2021). SenseFly eBeeX İHA ile Üretilen Ortofotonun Konum Doğruluğunun İncelenmesi. *Türkiye İnsansız Hava Araçları Dergisi*, *3*(2), 65-68.
22. Smith, D., & Heidemann, H. K. (2015). New standard for new era: Overview of the 2015 ASPRS positional accuracy standards for digital geospatial data. *Photogrammetric Engineering & Remote Sensing*, *81*(3), 173-176.
23. Snavely, N., Seitz, S. M., & Szeliski, R. (2008). Modeling the world from internet photo collections. *International journal of computer vision*, *80*(2), 189-210.
24. Westoby, M. J., Brasington, J., Glasser, N. F., Hambrey, M. J., & Reynolds, J. M. (2012). 'Structure-from-Motion'photogrammetry: A low-cost, effective tool for geoscience applications. *Geomorphology*, *179*, 300-314.
25. Eroğlu, M., & Narin, Ö. G. (2021). İnsansız hava aracı ile üretilen Sayısal Yükseklik Modeli (SYM) ile Google Earth ve HGM Küre verilerinin karşılaştırılması. *Politeknik Dergisi*, *24*(2), 545-551.
26. Yakar, M., Orhan, O., Ulvi, A., Yiğit, A. Y., & Yüzer, M. M. (2015). Sahip Ata Külliyesi Rölöve Örneği. *TMMOB Harita ve Kadastro Mühendisleri Odası*, *10*.
27. Morgan, J. A., & Brogan, D. J. (2016). How to VisualSFM. *Dep. Civ. Environ. Eng. Color. State Univ. Fort Collins, Color.*
28. Cook, K. L. (2017). An evaluation of the effectiveness of low-cost UAVs and structure from motion for geomorphic change detection. *Geomorphology*, *278*, 195-208.
29. Maes, W. H., & Steppe, K. (2019). Perspectives for remote sensing with unmanned aerial vehicles in precision agriculture. *Trends in plant science*, *24*(2), 152-164.
30. Peña-Villasenín, S., Gil-Docampo, M., & Ortiz-Sanz, J. (2019). Professional SfM and TLS vs a simple SfM photogrammetry for 3D modelling of rock art and radiance scaling shading in engraving detection. *Journal of Cultural Heritage*, *37*, 238-246.
31. Alptekin, A., Çelik, M. Ö., Doğan, Y., & Yakar, M. (2019). Mapping of a rockfall site with an unmanned aerial vehicle. *Mersin Photogrammetry Journal*, *1*(1), 12-16.
32. Ulvi, A., Yakar, M., Yiğit, A., & Kaya, Y. (2019). The use of photogrammetric techniques in documenting cultural heritage: The Example of Aksaray Selime Sultan Tomb. *Universal Journal Of Engineering Science*, *7*(3), 64-73.
33. Kılınçoğlu, D. B. (2016). *Farklı insansız hava araçları ile elde edilen görüntülerin otomatik fotogrametrik yöntemlerle değerlendirilmesi ve doğruluk analizi* (Doctoral dissertation, Fen Bilimleri Enstitüsü).

Mersin Photogrammetry Journal
https://dergipark.org.tr/en/pub/mephoj
e-ISSN 2687-654X

3D modeling of car parts by photogrammetric methods: Example of brake discs

Engin Kanun [*1], **Ganime Melike Oğuz** [2], **Murat Yakar** [3]

[1]*Mersin University, Faculty of Engineering, Department of Mechanical Engineering, Mersin, Türkiye*
[2]*ESC Engineering, Geomatics Engineer, Adana, Türkiye*
[3]*Mersin University, Faculty of Engineering, Department of Geomatics Engineering, Mersin, Türkiye*

Keywords
Reverse Engineering
3D modeling
Photogrammetry
Brake discs

Research/Review Article
DOI:10.53093/mephoj.1131619

Received:16.06.2022
Accepted:04.07.2022

Abstract

Re-measurement of existing, manufactured parts and re-creation of 3D models of these parts brought about the concept of reverse engineering. Reverse engineering has become a frequently applied and utilized concept in processes such as repairing damaged parts, improving used parts, and making new designs based on old parts. One of the main reverse engineering methods widely used by many engineering branches is photogrammetry. Photogrammetry, which includes a wide range of applications from professional cameras to mobile phones, is divided into branches such as terrestrial photogrammetry, aerial photogrammetry and underwater photogrammetry. The basis of all these categories is the concept of making measurements of a part, structure or region and modeling them in 3D, even if they involve different equipment and instruments. In this study, the 3D model of a rear brake disc of a personal passenger car was obtained using mobile photogrammetric methods. In the results section, the applicability of the method was examined in terms of cost, time and accuracy, together with the results of the accuracy analysis. It has been shown that the mobile photogrammetry method can provide easy applicability, low cost and high accuracy of 0.88 mm.

1. Introduction

The popularity of reverse engineering applications is increasing progressively. Not only engineers, but also many professions such as architects, archaeologists, biologists, medics and historians use these applications which are becoming more and more comprehensive and developing [1-7].

Some of the examples of reverse engineering applications of mechanical engineering are 3D modeling and prototyping of a damaged helical gear [8], 3D modeling and simulation of milling tools [9], 3D model generation of a plate and determination of heat transfer properties [10], 3D modeling and deformation analysis of roof bolts [11], simulating the resistance spot welding process of a panel and deformation analysis [12], 3D modeling of antique machines and transferring them to future generations [13] and 3D modeling and flow analysis of a damaged turbocharger [14].

The aviation industry is another branch that utilizes reverse engineering methods. For instance: 3D modeling of micro-grooved wings and investigation of their flow characteristics [15], assembly inspection of large aircrafts with non-contact measurements [16], investigation of airframes and aerodynamic surfaces using LiDAR sensors [17].

Another branch in which reverse engineering applications are used is the maritime sector. There are many reverse engineering applications utilized in shipyards, marinas, offshore platforms, and ships under cruising. Ship hull shape modelling, hull shape measurements and corrections, damage analysis and repairs with the application of photogrammetry based systems [18], 3D modeling of the main drive propeller shaft housing and detection of manufacturing defects [19], hull form and propeller modeling and their comparison with project data [20-22], 3D modeling of submarines [23], production of a prototype of a fishing boat using photogrammetric and terrestrial laser

* **Corresponding Author**

*(ekanun@mersin.edu.tr) ORCID ID 0000-0002-2369-5322
(melikoguzz@gmail.com) ORCID ID 0000-0003-0241-6870
(myakar@mersin.edu.tr) ORCID ID 0000-0002-2664-6251

Cite this article

Kanun, E., Oğuz, G. M., & Yakar, M. (2022). 3D modeling of car parts by photogrammetric methods: Example of brake discs. *Mersin Photogrammetry Journal, 4(1), 07-13*

scanning methods [24], 3D modeling of underwater remains of historic ships [25], overall efficiency assessment and hydrodynamic performance calculations of a trawler propulsion system [26] can be given as examples of the concept of using reverse engineering applications in the maritime industry.

There are many reverse engineering applications for the documentation of cultural heritage. Geomatics engineers, city planners, historians, archaeologists and anthropologists take part in the documentation of cultural heritage and carry out scientific studies. In all these processes, it is necessary to avoid damaging the objects while performing the measurements and 3D modeling of the artifacts. For this reason, reverse engineering studies are carried out with advanced methods such as terrestrial photogrammetry, aerial photogrammetry, underwater photogrammetry, mobile photogrammetry, terrestrial laser scanning, underwater laser scanning, and aerial laser scanning. 3D modeling of a historic castle [27], documentation of historical caravansaries by digital close range photogrammetry [28], 3D modeling of a mausoleum using a terrestrial laser scanner [29] are some examples of documenting cultural heritage using reverse engineering methods.

In this study, close range photogrammetry, which is one of the reverse engineering methods mentioned above, was used. Close range photogrammetry includes a calibrated camera, marked points on the object, and computer as shown in the ‘‘Fig. 1’’.

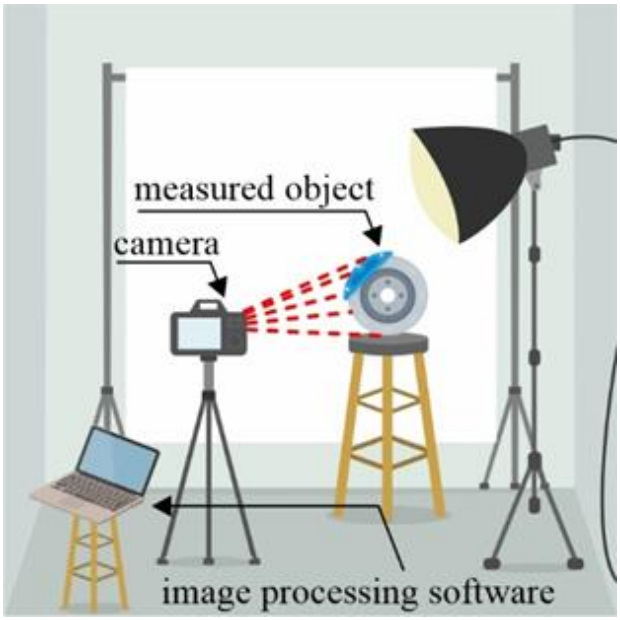

Figure 1. Photogrammetric measurement components

Marked points are pasted on the object to be measured. The camera takes several photos of objects from different directions to create two-dimensional digital images. Using picture recognition technology, the location of marked points can be determined in the computer [30]. The coordinates of marked points, as well as the camera's position and orientation, can be calculated using the correlation equation and mathematical model [31].

High measuring accuracy is one of the most essential characteristics of close-range photogrammetry. In the case of a high configuration, relative accuracy in the single-camera measuring system can reach 5µm +5µm/m. High efficiency is another characteristic of close-range photogrammetry. Obtaining data on tens of thousands of data points in a short period of time is possible using this method. Another remarkable feature of close-range photogrammetry is stable performance. Even in the presence of adverse conditions such as vibration, high temperature, high pressure, and hazardous locations, high accuracy readings can be achieved. Measuring without contact is another significant property of close-range photogrammetry, thus the object to be measured is not damaged at all [30].

One of the most important inventions of mankind, which has made many inventions from the past to the present, is undoubtedly the automobile. In this industry, which has been open to development and innovation throughout history, the safety systems of vehicles are also being improved day by day. When it comes to automobile safety systems, one of the first and most significant systems that comes to mind is brake systems. Currently, the most used braking system is the system consisting of disc (rotor), caliper, piston and pads as shown in the ‘‘Fig. 2’’.

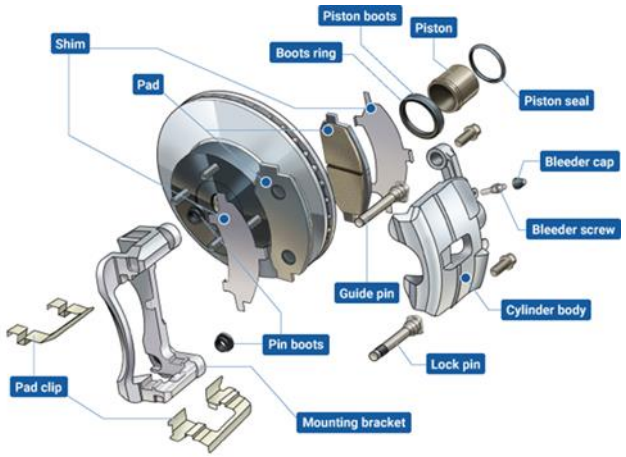

Figure 2. Components of disc brakes [32]

Disc brake rotors rotate with the wheels, and brake pads attached to the brake calipers clamp down on these rotors to stop or slow the wheels. Friction is created when the brake pads press against the rotors, converting kinetic energy to thermal energy. This thermal energy produces heat, but because the major components are exposed to the atmosphere, the heat is effectively diffused. This heat-dissipating feature helps to prevent brake fade, which is when the heat affects braking performance. Another benefit of disc brakes is its resistance to water fade, which happens when water on the brakes reduces braking force dramatically. The rotor rotates at high rates as the vehicle is moving, and this rotational motion discharges the water from the rotors, resulting in a consistent braking force [32].

The aim of this study is to investigate whether automobile parts can be modeled in 3D by mobile photogrammetry method, which is the process of creating a 3D model of an object by taking photos from different angles via a mobile phone. In this study, the right rear brake disc of the 2012 model Citroën C4 B7 has

been examined. First, the brake disc was disassembled from the vehicle. Photographs were taken to obtain the 3D model, and finally, the obtained model was examined. The pre-measurements on the brake disc and the dimensions of the created 3D CAD model were compared, accuracy analysis was made and presented in the results section.

As a result, the method used was examined in terms of accuracy, cost, time and applicability. Since the obtained 3D model can be used in various works such as maintenance-repair, restoration, prototyping, product development, and improvement of old designs, this study has the feature of being a guide for those who want to do this job in the market [33-35].

2. Method

In this paper, smartphone-based photogrammetric survey was implemented to obtain the 3D model of the right rear brake disc which is examined in this study. The brake disc was dismantled from a 2012 Citroën C4 B7 1.6 VTi car.

Figure 3. Brake disc removal step

Although the front brake discs of this vehicle are ventilated, the rear discs are solid. Solid brake discs, which have less design details than ventilated brake discs, are more suitable for modeling with photogrammetric methods. For this reason, modeling ventilation ducts and holes correctly in 3D would give low accuracy with the photogrammetric method.

Figure 4. Front and rear view of disassembled brake disc

This study consists of two phases such as field work and office work. During the field work, photogrammetric images were captured with the aim of obtaining the 3D model of the brake disc. At the stage of office work, the photos were uploaded to the computer for processing and a 3D model was obtained.

2.1. Specifications and Features of the Camera

Digital images of the brake disc were acquired by using Samsung Galaxy S10 mobile phone. The mobile phone has three rear cameras. The main camera of the phone has 12- megapixels with a 5.6x4.2 mm sensor size. Auto-focusing and focusing at infinity settings were applied. The minimum focusing distance of the camera is 0.10 m and the hyperfocal distance of the camera is 3.60 m. The lens of the camera has a focal length of 4.32 mm and (f/1.5) aperture. Focal length (35 mm eq.) is 27.7714 mm. In addition, the lens has a 66.3° horizontal field of view and 52.2° vertical field of view. Magnification factor was 1x for all photos taken. In addition to all these, camera calibration was performed and the calibration coefficients of the camera were calculated.

Figure 5. Smartphone used for data acquisition

2.2. Camera Calibration

One of the requirements for obtaining a highly accurate photogrammetric model is camera calibration. As a result of the camera calibration, the camera distortion parameters of the lens are calculated. Thus, depth maps are obtained more accurately and high precision is achieved.

For this reason, within the scope of the study, photographs of the chessboard seen in "Fig. 6" were taken from different angles and transferred to the computer. The photos taken were processed in the camera calibration module of Agisoft Metashape Professional software and the distortion parameters were calculated.

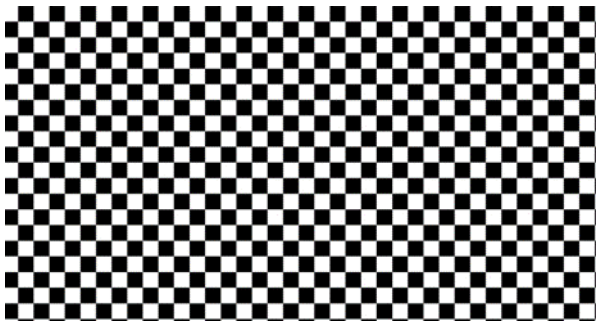

Figure 6. Chessboard used for camera calibration

The results of the camera calibration parameters obtained from calibration process shown at the "Table 1":

Table 1. Camera calibration results

Parameter	Value	Parameter	Value
f	3095.89482	**cx**	-34.863
k1	0.346132	**cy**	-2.22197
k2	-2.4963	**p1**	0.000972003
k3	6.41376	**p2**	0.000524342
k4	-5.52763	**b1**	-0.899219
		b2	-1.56922

2.3. Data Acquisition

The front and rear faces of the brake disc were modeled separately and then assembled. For this reason, 191 photographs of the brake disc, which was disassembled from the car, were taken from different angles and from different distances as shown in ''Fig. 7 and 8''. A portable spotlight was used to provide the right lighting during the photo shoots. Blurry photos, flash light, optical stabilization, digital zoom, and fish-eye lenses were avoided in order to produce better results.

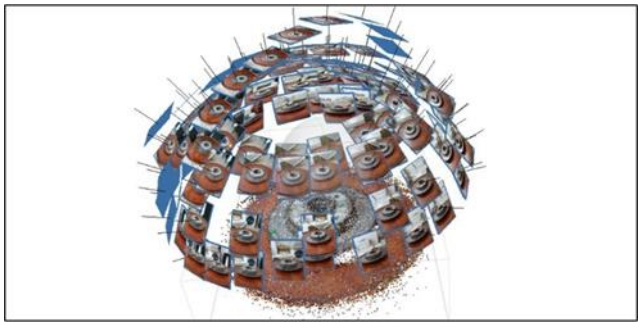

Figure 7. Camera stations configuration of brake disc (front)

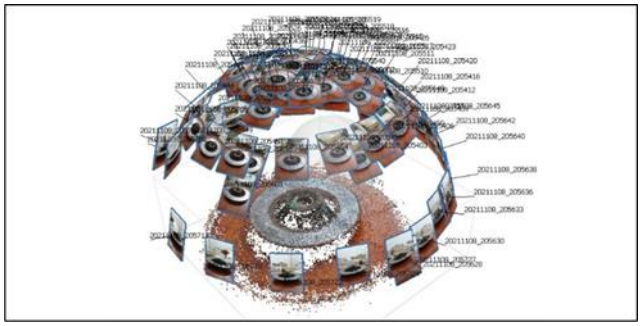

Figure 8. Camera stations configuration of brake disc (rear)

2.4. Data Processing

After the completion of the field work, the office work phase was initiated. During the office phase of the study, 191 of the images were processed at Agisoft Metashape Professional Software. Two user tie points were marked on every component of the brake disc to submit an accurate triangulation to the photos. Then, by taking precise measurements on the parts of the brake disc, predefined positioning and scale constrains were generated with two user tie points that marked before as seen in the ''Fig. 9''. Generic block type option was selected with the aim of helping the triangulation process. Since the camera calibration parameters have already been calculated, 'Keep camera calibration' option was selected for aerotriangulation process. The points (numbered 1 to 4), shown in yellow in Figure 9, are marked in all photographs so that the camera positions are accurately determined and the point cloud data is as noise-free as possible.

Figure 9. User tie points and scale constrains of the brake disc

After the aerotriangulation process, 3D point cloud data generation step was initiated. Colored point cloud was constructed by selecting the options of 1 pixels point sampling, no-compression, and visible colors for color source. On the obtained point cloud data, the points belonging to the unwanted regions were roughly cleaned. In this way, unnecessary processing power usage and time wastage were avoided during the process.

After cleaning the redundant points in the sparse point cloud data, dense point cloud data was generated applying moderate depth filtering. For the front side of the brake disc, sparse point cloud data contains 143,040 points, while dense point cloud data contains 1,266,657 points. As for the rear side, sparse point cloud data contains 83,821 points, while dense point cloud data contains 1,375,748 points. Sparse and dense point cloud data of the front and rear surfaces of the brake disc are shown in ''Fig. 10 and 11''.

Figure 10. Sparse and dense point cloud data (front)

Figure 11. Sparse and dense point cloud data (rear)

During the mesh building process, source data was selected as dense cloud. Surface type was selected as arbitrary (3D) and high-quality face count was applied. Interpolation was enabled and calculate vertex colors option was marked. All these processes were applied separately for the front and rear surfaces of the brake disc, and the final version of the 3D brake disc model was obtained by combining the 2 models obtained at the end.

3. Results and Discussion

"Fig. 12" shows the 3D photogrammetric model of the brake disc. There are 467,929 total Triangulated Irregular Networks (TIN) grids on the model.

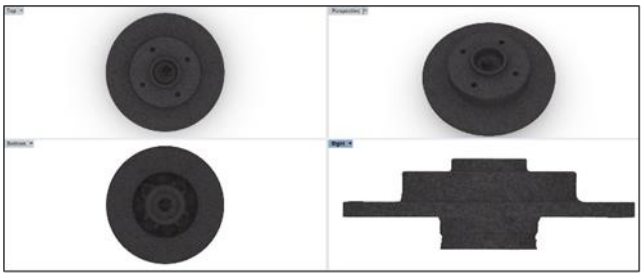

Figure 12. 3D solid model of the brake disc from different views

Considering the significance of design verification in the overall reverse engineering phase, few, if any, publications on part-to-CAD reverse engineering discuss modeling accuracy [36]. After obtaining the 3D photogrammetric model of the brake disc, accuracy analysis was performed on the model. The measurements taken on the brake disc before starting the photo acquisition were compared with the measurements of the 3D photogrammetric model obtained as a result of the study. "Fig. 13" presents the lengths compared on the object. The root mean square error values obtained are presented in "Table 2":

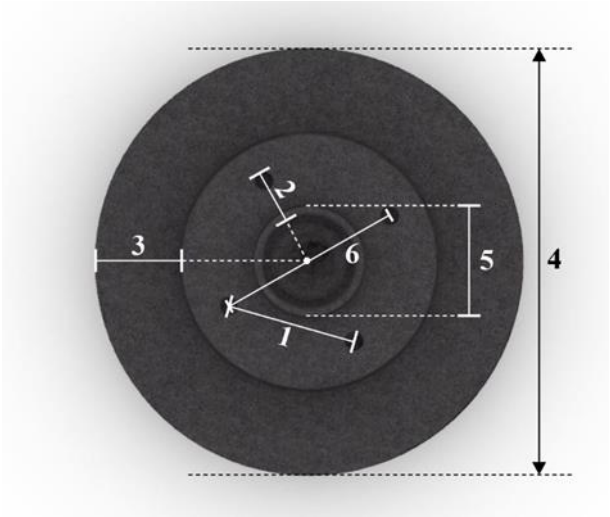

Figure 13. The lengths compared on the object

According to "Table 2", the 3D model of the brake disc has a total root mean square error (RMSE) of **0.88 mm**.

In addition to the dimensional accuracy analysis, point deviation analysis was also performed. The deviation between the obtained point cloud data and the surface of the solid model was analyzed separately for the front and rear faces of the brake disc. "Fig. 14" and "Fig. 15" present the results of the point deviation analysis of the front and rear surfaces of the brake disc. As can be seen in the figures, most of the points overlap with the solid model surface. Holes and sharp edges on the object are the parts where point deviations are most evident. According to the color scale, the blue colored dots exactly overlap with the surface, while the red colored dots are the places with relatively high deviations.

Table 2. Accuracy assessment results [in mm]

Length	Real	Model	V	VV
1	81	81.4	0.4	0.16
2	35	33.8	1.2	1.44
3	53	54.1	1.1	1.21
4	247	246.4	0.6	0.36
5	70	70.8	0.8	0.64
6	95	94.1	0.9	0.81

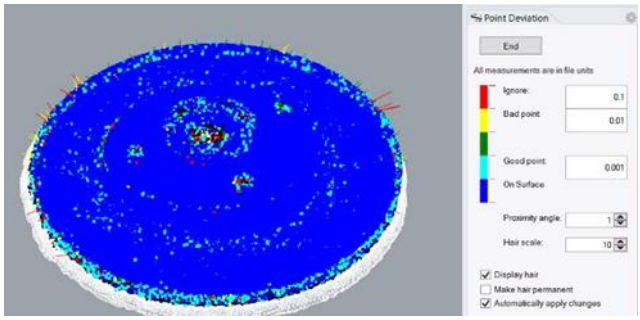

Figure 14. Point deviation analysis of the front side

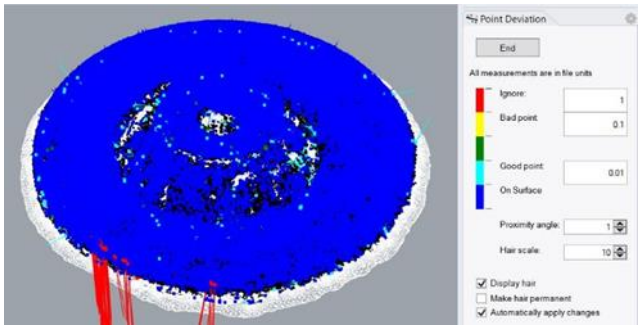

Figure 15. Point deviation analysis of the rear side

Keypoints density average, calculated by the software, is 5541 points per image. Reprojection error is 0.85 pixels. "Table 3" presents the position uncertainties of computed images.

Table 3. The position uncertainties of computed images

	X [units]	Y [units]	Z [units]
Minimum	0.0012	0.00106	0.00144
Mean	0.00352	0.00347	0.00384
Maximum	0.01309	0.01622	0.02073

4. Conclusion

To summarize, the concept of reverse engineering was mentioned in this study. Examples of the use of photogrammetry, which is one of the most frequently

used reverse engineering methods, in the literature are given. It has been shown that car parts can be modeled with high accuracy and in three dimensions by photogrammetric methods. In the next study, it is planned to model the same part with a handheld laser scanner. The results will be compared and it will be discussed which method is more suitable for modeling such parts. This study also has the feature of being a guide for those who will do this job in the market.

Acknowledgement

The authors would like to thank the members of Mersin University Department of Geomatics Engineering for their contribution to this study.

Author contributions

Engin Kanun: Data curation, Writing-Original draft preparation, Software, Validation. **Ganime Melike Oğuz:** Visualization, Investigation, Writing-Reviewing and Editing. **Murat Yakar:** Conceptualization, Methodology, Software.

Conflicts of interest

The authors declare no conflicts of interest

References

1. Yakar, M., Murat Yılmaz, H., Yıldız, F., Zeybek, M., Şentürk, H., & Çelik, H. (2009). Silifke-Mersin Bölgesinde Roma Dönemi Eserlerinin 3 Boyutlu Modelleme Çalışması ve Animasyonu. *Jeodezi ve Jeoinformasyon Dergisi*, (101).
2. Şanlıoğlu, İ., Zeybeka, M., & Karauğuzb, G. (2013). Photogrammetrıc survey and 3D modelıng of Ivrız rock relief in LATE Hittite Era. *Mediterranean Archaeology & Archaeometry*, *13*(2).
3. Yakar, M., & Doğan, Y. (2018). GIS and three-dimensional modeling for cultural heritages. *International Journal of Engineering and Geosciences (IJEG)*, *3*(2), 50-55.
4. Unal, M., Yakar, M., & Yildiz, F. (2004, July). Discontinuity surface roughness measurement techniques and the evaluation of digital photogrammetric method. In *Proceedings of the 20th international congress for photogrammetry and remote sensing, ISPRS* (Vol. 1103, p. 1108).
5. Yakar, M., Yılmaz, H. M., Güleç, S. A., & Korumaz, M. (2009). Advantage of digital close range photogrammetry in drawing of muqarnas in architecture. Information Technology Journal, 8(2), 202-207.
6. Alyilmaz, C., Yakar, M., & Yilmaz, H. M. (2010). Drawing of petroglyphs in Mongolia by close range photogrammetry. *Scientific Research and Essays*, *5*(11), 1216-1222.
7. Yılmaz, H. M., Karabörk, H., & Yakar, M. (2000). Yersel fotogrametrinin kullanım alanları. *Niğde Üniversitesi Mühendislik Bilimleri Dergisi*, *4*(1), 1.
8. Şahin, İ., Şahin, T., & Gökçe, H. (2017). Hasarlı Dişlilerin Tersine Mühendislik Yaklaşımıyla Yeniden Oluşturulması. *Düzce Üniversitesi Bilim ve Teknoloji Dergisi*, *5*(2), 485-495.
9. Che, J., Zhang, Y., Wang, H., Liu, Y., Du, M., Ma, S., ... & Suo, C. (2021). A novel method for analyzing working performance of milling tools based on reverse engineering. *Journal of Petroleum Science and Engineering*, *197*, 107987.
10. Zhang, L., Yuan, J., He, S., Huang, S., Xiong, S., Shi, T., & Xuan, J. (2021). Contact heat transfer analysis between mechanical surfaces based on reverse engineering and FEM. *Tribology International*, *161*, 107097.
11. Singh, S. K., Raval, S., & Banerjee, B. (2021). A robust approach to identify roof bolts in 3D point cloud data captured from a mobile laser scanner. *International Journal of Mining Science and Technology*, *31*(2), 303-312.
12. Liu, X., Wei, Y., Wu, H., & Zhang, T. (2020). Factor analysis of deformation in resistance spot welding of complex steel sheets based on reverse engineering technology and direct finite element analysis. *Journal of Manufacturing Processes*, *57*, 72-90.
13. LaRocco, J., & Paeng, D. G. (2020). A functional analysis of two 3D-scanned antique pistols from New Zealand. *Virtual Archaeology Review*, *11*(22), 85-94.
14. Kanun, E. (2021). Using photogrammetric modeling in reverse engineering applications: Damaged turbocharger example. *Mersin Photogrammetry Journal*, *3*(1), 21-28.
15. Chitsaz, N., Siddiqui, K., Marian, R., & Chahl, J. (2021). An experimental study of the aerodynamics of micro corrugated wings at low Reynolds number. *Experimental Thermal and Fluid Science*, *121*, 110286.
16. Liang, B., Liu, W., Liu, K., Zhou, M., Zhang, Y., & Jia, Z. (2021). A Portable Noncontact Profile Scanning System for Aircraft Assembly. *Engineering*.
17. Aldao, E., González-Jorge, H., & Pérez, J. A. (2021). Metrological comparison of LiDAR and photogrammetric systems for deformation monitoring of aerospace parts. *Measurement*, *174*, 109037.
18. Koelman, H. J. (2010). Application of a photogrammetry-based system to measure and re-engineer ship hulls and ship parts: An industrial practices-based report. *Computer-Aided Design*, *42*(8), 731-743.
19. Deja, M., Dobrzyński, M., & Rymkiewicz, M. (2019). Application of reverse engineering technology in part design for shipbuilding industry. *Polish Maritime Research*, 26(2), 126–133. https://doi.org/10.2478/pomr-2019-0032
20. Kanun, E., & Yakar, M. (2021). Mobıle phone-based photogrammetry for 3D modelıng of shıp hulls. *Mersin University Journal of Maritime Faculty*, *3*(1), 9-16.
21. Ackermann, S., Menna, F., Scamardella, A., & Troisi, S. (2008, July). Digital photogrammetry for high

precision 3D measurements in shipbuilding field. In *6th CIRP International Conference on ICME-Intelligent Computation in Manufacturing Engineering*.
22. Tassetti, N., Martelli, M., & Buglioni, G. (2015, June). Reverse engineering techniques for trawler hull 3D modelling and energy efficiency evaluation. In *Proc of NAV 2015 18th International Conference on Ships and Shipping Research* (pp. 24-26).
23. Burdziakowski, P., & Tysiac, P. (2019). Combined close range photogrammetry and terrestrial laser scanning for ship hull modelling. *Geosciences*, *9*(5), 242. https://doi.org/10.3390/geosciences9050242
24. Abbas, M. A., Lichti, D. D., Chong, A. K., Setan, H., Majid, Z., Lau, C. L., ... & Ariff, M. F. M. (2017). Improvements to the accuracy of prototype ship models measurement method using terrestrial laser scanner. *Measurement*, *100*, 301-310. https://doi.org/10.1016/j.measurement.2016.12.053
25. Menna, F., & Nocerino, E. (2014). Hybrid survey method for 3D digital recording and documentation of maritime heritage. *Applied Geomatics*, *6*(2), 81-93. https://doi.org/10.1007/s12518-011-0074-9
26. Martelli, M., Vernengo, G., Bruzzone, D., & Notti, E. (2016, June). Overall efficiency assessment of a trawler propulsion system based on hydrodynamic performance computations. In *The 26th International Ocean and Polar Engineering Conference*. OnePetro.
27. Çelik, M. Ö., Yakar, İ., Hamal, S., Oğuz, G. M., & Kanun, E. (2020). Sfm tekniği ile oluşturulan 3B modellerin kültürel mirasın belgelenmesi çalışmalarında kullanılması: Gözne Kalesi örneği. *Türkiye İnsansız Hava Araçları Dergisi*, *2*(1), 22-27.
28. Yakar, M., & Yılmaz, H. M. (2008). Kültürel miraslardan tarihi Horozluhan'in fotogrametrik rölöve çalişmasi ve 3 boyutlu modellenmesi. *Selçuk Üniversitesi Mühendislik, Bilim ve Teknoloji Dergisi*, *23*(2), 25-33.
29. Alptekin, A., Çelik, M. Ö., & Yakar, M. (2019). Anıtmezarın yersel lazer tarayıcı kullanarak 3B modellenmesi. *Türkiye Lidar Dergisi*, *1*(1), 1-4.
30. Jing, X., Zhang, C., Sun, Z., Zhao, G., & Wang, Y. (2015, April). The technologies of close-range photogrammetry and application in manufacture. In *3rd International Conference on Mechatronics, Robotics and Automation* (pp. 988-994). Atlantis Press.
31. Huang, G. P. (2005). Study on the key technologies of digital close range industrial photogrammetry and applications. *Tianjin: Tianjin University*.
32. Ingeniería y la mecánica (2019). Disc brakes: construction, working principle, types, and rotor materials.
33. Şahin, İ., Şahin, T., & Gökçe, H. (2017). Hasarlı Dişlilerin Tersine Mühendislik Yaklaşımıyla Yeniden Oluşturulması. *Düzce Üniversitesi Bilim ve Teknoloji Dergisi*, *5*(2), 485-495.
34. Saiga, K., Ullah, A. S., & Kubo, A. (2021). A Sustainable Reverse Engineering Process. *Procedia CIRP*, *98*, 517-522. https://doi.org/10.1016/j.procir.2021.01.144.
35. Li, L., Li, C., Tang, Y., & Du, Y. (2017). An integrated approach of reverse engineering aided remanufacturing process for worn components. *Robotics and Computer-Integrated Manufacturing*, *48*, 39-50.
36. Ingle, K. A. (1994). *Reverse engineering*. McGraw-Hill Professional Publishing.

Mersin Photogrammetry Journal

https://dergipark.org.tr/en/pub/mephoj

e-ISSN 2687-654X

Determination of Ayancık Stream Basin and its morphometric parameters

Emine Müjgan Ergene[1], Elnaz Najatishendi *[1] Melis Uzar [1] Füsun Balık Şanli [1]

[1] *Yildiz Technical University, Geomatics Engineering, Türkiye*

Keywords
Remote sensing
DEM
Basin
Morphometry
Flow
Flood
GIS

Research Article
DOI:10.53093/mephoj.1123641

Received: 31.05.2022
Accepted: 05.07.2022

Abstract

As a result of the increase in the negative effects of climate change, many natural disasters such as drought, forest fires, and floods are experienced all over the world. In Türkiye, especially in the Black Sea region, floods and overflows are frequently seen due to excessive precipitation. The use of current data obtained from the land management information system in the disaster management information system increases the accuracy of the predictability of disasters and ensures their sustainability. For this reason, the accuracy and up-to-date data obtained from the land management information system are important. Storage, modeling, querying, analysis, and tracking model has created for local and private administrations thanks to the acquisition of data by remote sensing and photogrammetry methods and their integration with GIS. Thus, natural disasters caused by the negative effects of climate change can be prevented. It is necessary to model the basin in terms of geological, geomorphological, and hydrographic and to create a basin management model, especially to predict, monitor, and take precautions for flood and overflow events. In this study, the boundaries of the Ayancık Stream Basin, which is located on the Sinop Plateau and flows into the Black Sea by mostly flowing in the north-south direction, were determined and morphometric analyses of the basin were made. With the help of morphometric analysis, the hydrographic features of the Ayancık Stream Basin were determined.

1. Introduction

When the floods and overflows caused by heavy rain, snowmelt, ice, rain, tropical storm, or tropical surge and dam around the world are investigated, according to a study conducted on the global flood database site, 913 floods occurred in 169 countries between 2000 and 2015 and that 255 million people suffered from disasters has been reported to be affected (Figure.1) [1].

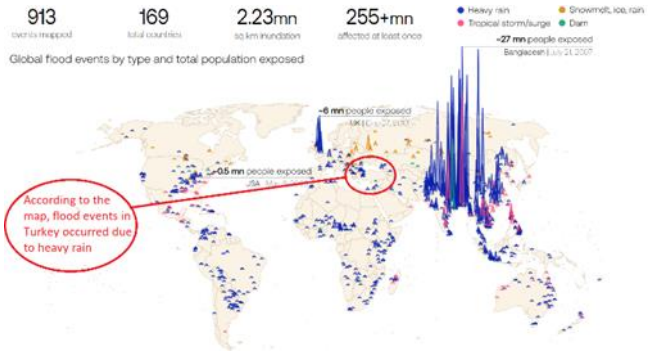

Figure 1. Flood disasters around the world between 2000 and 2015. Adopted from [1].

Within the scope of disaster management published by Disaster and Emergency Management Presidency (AFAD), in the 2019 year overview and nature-based event statistics report; it is stated that flood events increase as one goes from west to east and from south to north throughout Türkiye. In the report, the number of flood events that took place in Türkiye between 1950 and 2019 and their distribution by provinces were mapped [2]. In Figure 2, the number of floods/flood events that occurred in Türkiye between 1950 and 2019 are given on a provincial basis. In addition, Figure 2 shows that there were 31 floods in Sinop between 1950 and 2019.

Considering the available data, forecasting, monitoring, and analysis of flood and flood events is a multidisciplinary study. Therefore, watershed management prefers remote sensing and photogrammetry methods to save time and reduce costs by storing, querying, and analysing the geographical data of the region in a short time. By using the advantages of this method, it is ensured that the data is obtained up-to-date and with high accuracy in certain processes and that the change processes are analyzed and evaluated correctly. With the disaster information system to be

* **Corresponding Author**

(mujganergene@gmail.com) ORCID ID 0000-0002-1118-0006
*(elnaz.najatishendi@std.yildiz.edu.tr) ORCID ID 0000-0001-7901-5640
(auzar@yildiz.edu.tr) ORCID ID 0000-0003-0873-3797
(fbaliksanli@gmail.com) ORCID ID 0000-0003-1243-8299

Cite this article

Ergene, E. M., Najatishendi, E., Uzar, M., & Şanlı, F. B. (2022). Determination of Ayancık Stream Basin and its morphometric parameters. *Mersin Photogrammetry Journal, 4(1), 14-23*

established for this purpose, the geological, geomorphological, and hydrographic features of the basin are evaluated in a fast, accurate, and up-to-date manner.

Figure 2. 1950-2019 Number of flood events in Türkiye on a provincial basis. Adopted from [2].

Conditions such as the increase in temperature due to climate change and the melting of glaciers; natural processes such as precipitation amount and evaporation are affected. This situation causes irregular stream flow and varying drainage densities in stream basins. In such a case, it is necessary to determine and interpret the hydrographic characteristics of the basin to prevent natural disasters such as floods and overflows.

Morphometric analyses of the basin, such as; drainage network and density, the minimum and maximum height of the basin, the length of the stream, and its frequency that is the information used in determining the areas to be taken precautions in case of flood, choosing suitable regions for settlement, and making disaster planning. Morphometric analyses are examined in 3 groups: Linear Morphometry, Relief Morphometry, and Aerial Morphometry. In Table 1, the studies in which morphometric analyses were first published in the literature, and the author information are given.

By performing the basin boundary and morphometric analyses of the Sabuncular Stream in Rize province, Çayeli district, Ödeker B. and Türkoğlu N. (2020) determined that the basin has a high drainage density, causes the water to flow to the surface without being able to seep into the ground, the risk of surface erosion increases, and therefore the flood risk is high [10].

The flood disaster, which occurred due to heavy rain on August 11, 2021, in the Ayancık Stream, which is located in the Ayancık district of Sinop province in the Black Sea Region of Türkiye, caused many logs and vehicles to drift, damaged structures in the settlement, 47 buildings collapsed and 6 people died. It was seen that the most affected region in the flood disaster in Ayancık was the village of Babaçay. However, when the literature was examined, no study was found in which morphometric analyses of the basin area of the region were made.

In this study, ASTER GDEM data collected before the flood is utilized. The boundaries of the Ayancık Stream Basin, basin morphometric analyses, and hydrographic features were determined and performed. Thus the predictability of the flood disaster was investigated.

Table 1. Morphometric Parameters

Class	Morphometric Parameters	Formula	Author/Year
LINEAR	Stream Order (Nu)	Determined from Stream To Feature Vector data	First Horton, 1945 [3] As a Hierarchical Order Strahler, 1964[4]
	Stream Length (Lu)	Length of the stream	Hortan, 1945 [3] Strahler, 1964 [4]
	Mean Stream Length (Lsm)	Lsm = Lu/Nu Lu: Mean Stream Length of a given order (km) Nu: Number of Stream segment	Hortan, 1945[3]
	Stream Length Ratio (Rl)	Rl = Lu/Lu-1 Lu = total stream length of order Lu-1 = The Total Stream length of its next lower order	Hortan, 1945[3]
	Bifurcation Ratio (Rb)	Rb= Nu/Nu+1 Nu = Number of stream segments present in the given order Nu+1 = Number of segments of the next higher order	Schumn, 1956 [5]
RELIEF	Basin Relief (Bh)	Vertical distance between the lowest and highest points of basin	Schumn, 1956 [5]
	Relief Ratio (Rh)	Rh = Bh/Lb Bh = Basin Relief, Lb = Basin length	Schumn, 1956 [5]
	Hypsometric Curve (Hc)	Relative height/Relative area	Strahler, 1952 [8]
	Hypsometric Integral (Hi)	(Mean height - Minimum height)/ (Maximum height - Minimum Height)	Strahler, 1952 [8]
	Ruggedness Number (Rn)	Rn = Bh*Dd Bh=Basin Relief, Dd=Drainage density	Schumn, 1956 [5] Strahler, 1958 [9]
AREAL	Drainage Density (Dd)	Dd=L/A ; L=Total length of stream (km), A= Area of basin(km^2)	Hortan, 1945 [3]
	Stream Frequency (Fs)	Fs=Nu/A Nu=Total number of stream A= Area of basin	Hortan, 1945 [3]
	Texture Ratio (T)	T=N1/P N1=Total number of first order stream P=Perimeter of basin	Hortan, 1945 [3] Smith, 1950 [7]
	Form Factor (Rf)	$Rf=A/(Lb)^2$ A= area of basin, Lb=Basin length	Hortan, 1945 [3]
	Circulatory Ratio (Rc)	$Rc=4\pi A/P^2$; $\pi=3.14$ A= Area of basin , P=Perimeter of basin	Miller, 1953 [6]
	Elongation Ratio (Re)	$Re=\sqrt{(Au/\pi)}/Lb$, $\pi=3.14$ The length of circle's diameter with the area of the basin / The maximum length of the basin	Schumn, 1956 [5]
	Length of Overland Flow (Lg)	1/2Dd; Dd=Drainage density	Hortan, 1945 [3]
	Constant Channel Maintenance (C)	Lof = 1/Dd; Dd=Drainage density	Hortan, 1945 [3]

2. Study area

Ayancık, a district of Sinop province, was established at the foot of Ayancık Hill, where Ayancık Stream empties into the sea, facing the open sea. In the study area, the elevation increases towards the south, and the residential areas are gathered around the Ayancık stream and its tributaries. The maximum height of the basin area is 1869 m. In Figure 3, the study area and the Ayancık Stream Basin boundary are given.

3. Material and Method

The United States National Aeronautics and Space Administration (NASA) and the Ministry of Economy, Trade, and Industry (METI) of Japan jointly released Version 3 of the Advanced Spaceborne Thermal Emission and Reflection Radiometer (ASTER) Global Digital Elevation Model (GDEM) on August 5, 2019 Also, ASTERGDEMV3 data were provided as free satellite images. By using Digital Elevation Model (DEM) data, the watershed boundary was determined and morphometric analyses were made.

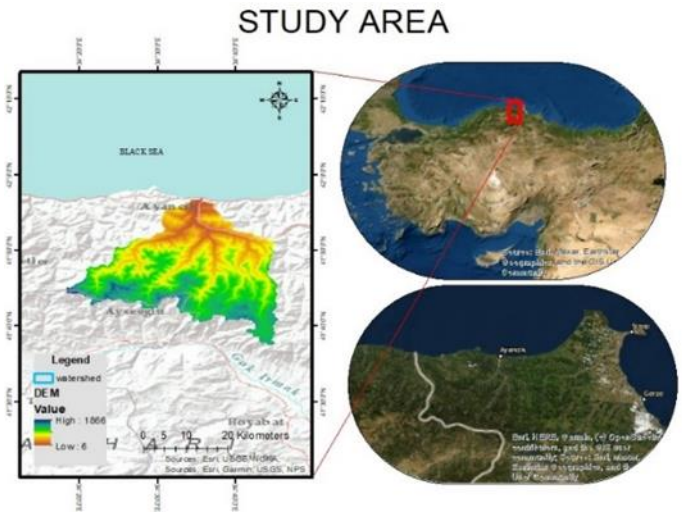

Figure 3. Study area and Ayancık Stream Basin Boundary

The improved Aster GDEM V3 adds additional stereo-pairs, improving coverage and reducing the occurrence of artifacts. The refined production algorithm provides improved spatial resolution and increased horizontal and vertical accuracy. The ASTER GDEM V3 maintains the GeoTIFF format and the same gridding and tile structure as V1 and V2, with 30-meter postings and 1 x 1-degree tiles [11].

In the first step, DEM data was transferred to geographic information systems and base maps were produced. In the DEM data transferred to the GIS software, firstly, the pixels without height information in the data were completed with the iteration method, which is the function renewal process. In the second step, flow direction, flow accumulation, watershed, and pressure are calculated. Stream Order stream indexes were calculated using the Strahler method with flow direction and Flow Accumulation obtained in the third step. In the next step, stream raster data is converted to vector data by calculating Stream to Feature using the calculated Stream Order. At this stage, the origin of the Ayancık Stream was determined as a point. By using the Flow Direction and the exit point of the Ayancık Stream, the water collection area-Basin area of the Ayancık Stream was determined by using the Watershed method.

The Basin boundary was obtained by converting the calculated Basin area from raster data type to vector data. According to the obtained basin boundary, Flow Direction, Flow Accumulation, Stream Order, and Stream to Feature analyses were mapped by mask. In addition, Stream Density was calculated using the line density method with Stream to Feature vector data. In Figure 4 workflow diagram is given.

Data such as basin area, length, and bifurcation rate required in morphometric analyses were obtained by using raster and vectorial data from the stream to feature, watershed and Fill-DEM.

3.1. Fill

In order to ensure the continuity of the drainage network to be created, the pixels in the data that do not contain height information are filled by iteration, which is a function iteration method, up to all pixels containing the determined z limit height value. In the study, the Z-limit value was chosen as 1m. With this correction, the discontinuities that may occur while determining the Flow Direction are prevented.

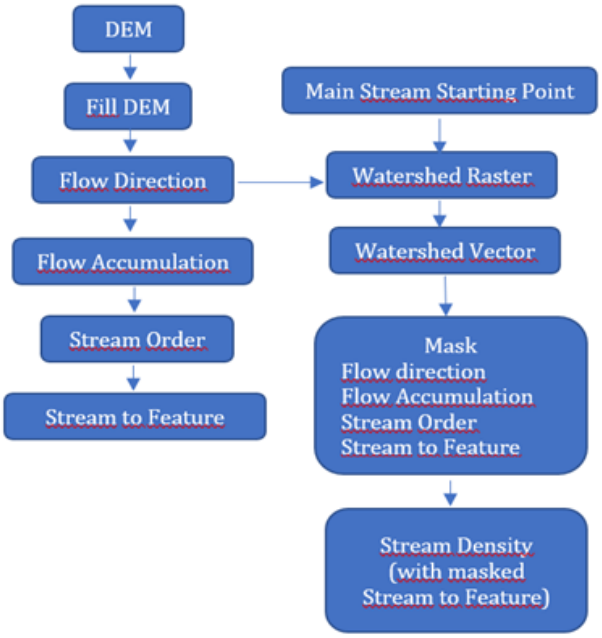

Figure 4. Flowchart

3.2. Flow Direction

By using the Digital Elevation Model, the transport movements of water channels and streams and materials can be calculated by using the flow directions in hydrology research. Each grid cell with a height value on the DEM moves towards one of the neighbouring grid cells that are lower than its own value in 8 possible directions: down, up, right, left, up right, up left, down right, and down left (Figure 5). Thus, the flow direction of the stream is determined by the 8-way flow model and numerical values are used to show the flow direction.

North-West	North	North-East	32	64	128
West		East	16		1
South-West	South	South-East	8	4	2

Figure 5. Flow Direction theory

3.3. Flow Accumulation

By using the determined flow direction, the collection areas of water are determined from the highest elevation value to the lowest elevation value. Flow Accumulation; It is calculated by the accumulated weight of all cells flowing to each low slope value in the Flow Direction, which is a raster image. Therefore, the cellular values of the flow network in the raster image obtained as a result of Flow Accumulation are the number of cells flowing into that cell (Figure 6). A threshold value can be selected to create a flow network by selecting cells with a high accumulated flow. Here, the threshold is the number of cells with the minimum flow and can be determined by examining the histogram of the raster data. If the threshold value is selected low, the density of the river

network will be high, and if high, the density of the river network will be low.

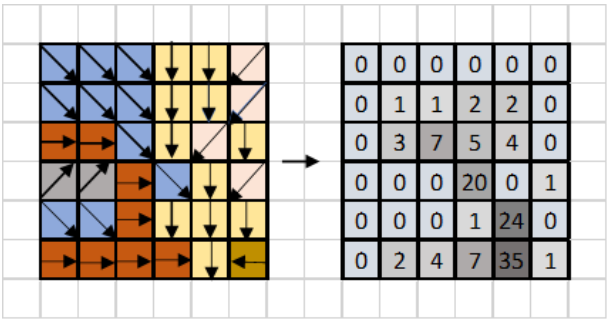

Figure 6. Flow Direction to Flow Accumulation

3.4. Stream Order and Feature

With the help of the flow density of the stream network determined by the selected threshold value and the flow direction of the stream, the main streamline and branches are found using the Strahler method. The found streamline and its branches are divided into indexes and numbered from smallest to largest. Since the obtained data is raster data and is defined with the stream line in the GIS environment, the raster data is converted to vector data and the necessary information for morphometric analyses such as the number of indexes and length of the stream is obtained.

The grading of stream tributaries was carried out for the first time by Horton's work. Horton's technique was developed with Strahler's work. While the tributaries are graded by the Strahler method, a stream bed with a small flow forms the 1st index. When two 1st directories merge, it creates the 2nd directory, when two 2nd directories merge, it creates the 3rd directory, and so on (Figure 7). In this case, an increase in index ranking is seen only when the same indexes are merged. There is no increase in index value when a smaller index is merged with a larger index [13].

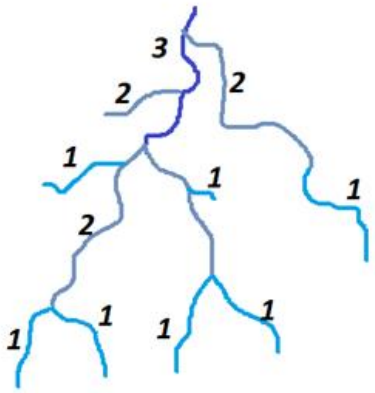

Figure 7. Strahler Method

3.5. Watershed

The lowest point along the basin boundary is the basin outlet. Therefore, the starting point of the Basin should be determined first. The basin boundary is obtained by determining the total flow area of the basin with the data of the basin starting point and the river flow direction.

3.6. Morphometric Parameters

The morphometric parameters that form the basis of the hydrological examination of the basin and provide the numerical expression of the ground surface consist of 3 groups: Linear Morphometry, Relief Morphometry, and Areal Morphometry. Table 2 includes morphometric parameters and their formulas.

Table 2. Formulas used in the calculation of morphometric parameters

Class	Morphometric Parameters	Formula
LINEAR	Stream Order (Nu)	Determined from Stream To Feature Vector data
	Stream Length (Lu)	Length of the stream
	Mean Stream Length (Lsm)	Lsm = Lu/Nu Lu: Mean Stream Length of a given order (km) Nu: Number of Stream segment
	Stream Length Ratio (Rl)	Rl = Lu/Lu-1 Lu = total stream length of order Lu-1 = The Total Stream length of its next lower order
	Bifurcation Ratio (Rb)	Rb= Nu/Nu+1 Nu = Number of stream segments present in the given order Nu+1 = Number of segments of the next higher order
RELIEF	Basin Relief (Bh)	Vertical distance between the lowest and highest points of basin
	Relief Ratio (Rh)	Rh = Bh/Lb Bh = Basin Relief, Lb = Basin length
	Hypsometric Curve (Hc)	Relative height/Relative area
	Hypsometric Integral (Hi)	(Mean height - Minimum height)/ (Maximum height - Minimum Height)
	Ruggedness Number (Rn)	Rn = Bh*Dd Bh=Basin Relief, Dd=Drainage density
AREAL	Drainage Density (Dd)	Dd=L/A ; L=Total length of stream (km), A= Area of basin(km²)
	Stream Frequency (Fs)	Fs=Nu/A Nu=Total number of stream A= Area of basin
	Texture Ratio (T)	T=N1/P N1=Total number of first order stream P=Perimeter of basin
	Form Factor (Rf)	$Rf=A/(Lb)^2$ A= area of basin, Lb=Basin length
	Circulatory Ratio (Rc)	$Rc=4\pi A/P^2$; π=3.14 A= Area of basin , P=Perimeter of basin
	Elongation Ratio (Re)	Re=√(Au/π)/Lb , π=3.14 The length of circle's diameter with the area of the basin / The maximum length of the basin
	Length of Overland Flow (Lg)	1/2Dd; Dd=Drainage density
	Constant Channel Maintenance (C)	Lof = 1/Dd; Dd=Drainage density

Basin linear morphometric parameters are, the number of streams, length, basin perimeter, basin length (L), basin width (B), Bifurcation Ratio (Rb), Length Ratio (RL), Surface Flow Length (Lo), and Texture Ratio (T) is [13].

The morphometric parameters formed by the spatial characteristics of the basins have a very important effect on the collection of precipitation falling into the basin and the accumulation of surface runoff. These parameters are; Drainage Density (Dd), Stream Frequency (Fs), Basin Shape (RF), and Length Ratio (Re) [13].

Relief morphometry of the landforms of the basin consists of features. These features are elevation, slope aspect, Basin Relief (Bh), Relief Ratio (Rh), Roughness Value (Rn), Flow Collection Time (Concentration Time) (Tc), Hypsometric Curve (Hc), and Hypsometric Integral (Hi) [13].

4. Results

4.1. Determination and analysis of the basin area

ASTER GDEM V3 raster image covering the study area; the elevation limit value (z-limit) is selected as 1 and iteratively corrected by filling the pixels that do not contain elevation information. The maximum elevation of DEM within the basin boundary was found to be 1869m and the minimum elevation of 10.7m by performing the mask operation with the basin boundary obtained by calculating the watershed. The Digital Elevation Model obtained by this process and the minimum and maximum elevation values of this model are shown in Figure 8.

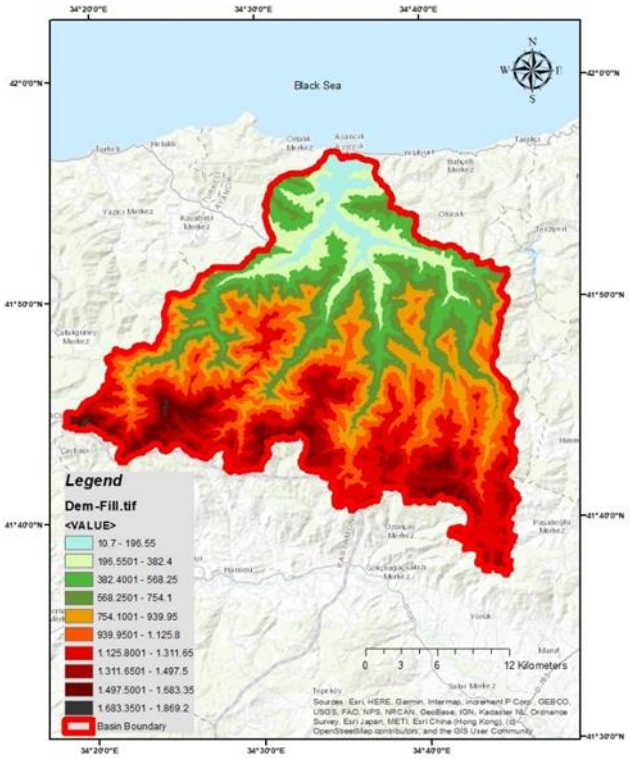

Figure 8. DEM Map

Flow direction was determined using the D8 (directional flow model) method on the obtained DEM. Flow Direction map created in 8 directions is shown in Figure 9.

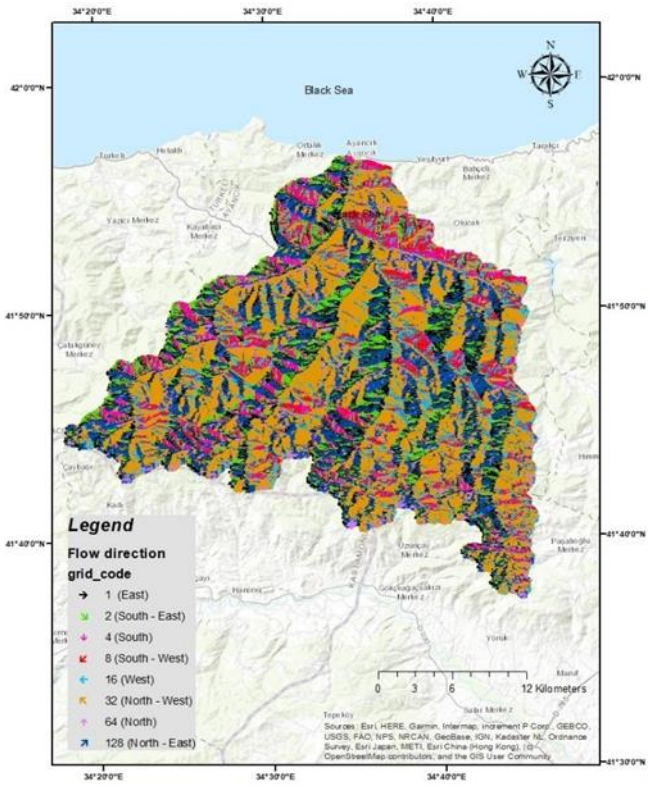

Figure 9. Flow Direction Map

In this study, drainage networks defined by the streams in the Ayancık Stream Basin were obtained and graded using the Strahler method (Figure 10). The drainage network of Ayancık Stream is divided into 5 indices. In this way, water collection areas and areas with drainage density could be determined (Figure 11). The pink areas formed on the river network in Figure 11 show that there are areas where the drainage density is high and that first of all precautions should be taken in case of a possible flood.

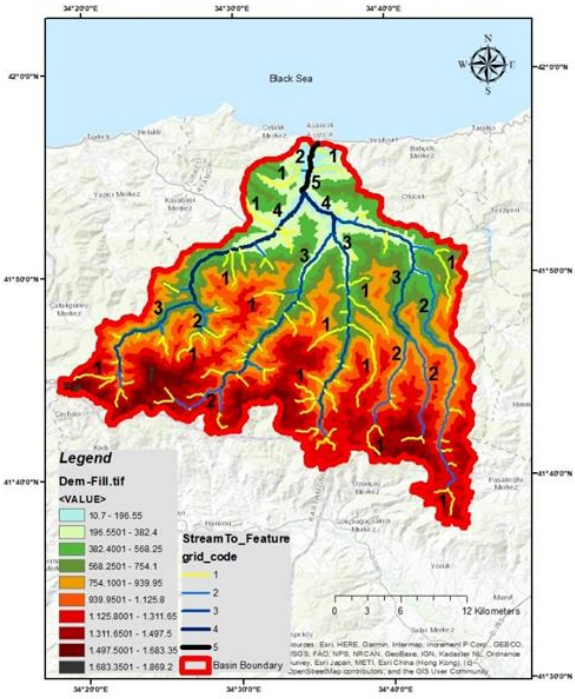

Figure 10. Stream Order Map

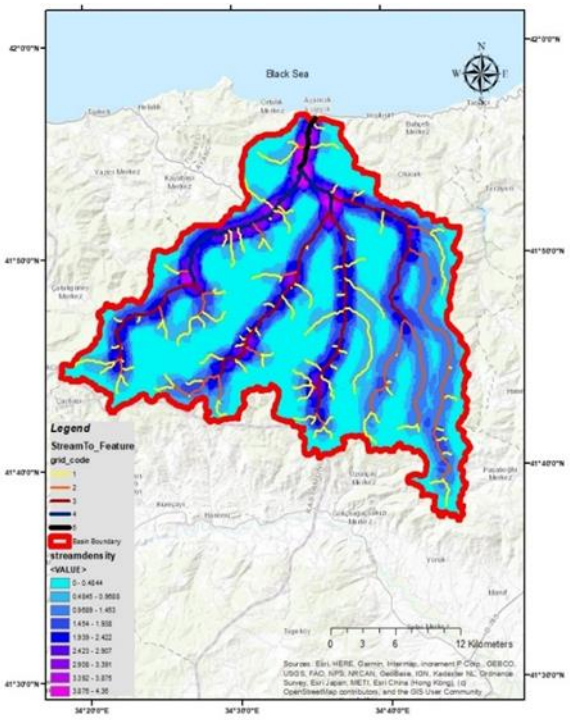

Figure 11. Drainage Density Map

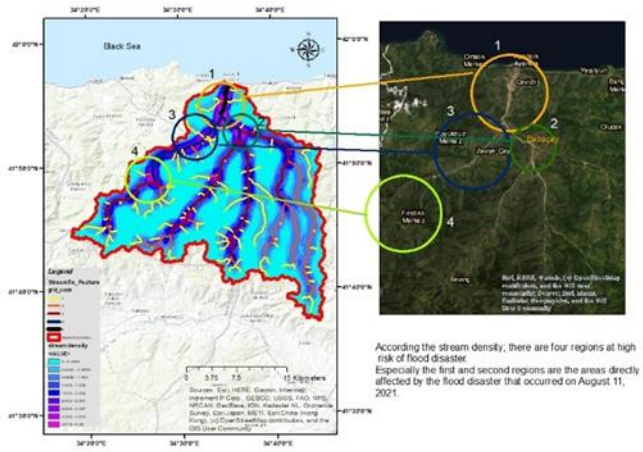

Figure 12. Drainage Density Map and Regional Comparison

In the drainage density map, 4 regions with high flood risk were determined (Figure 12). Since the Aster GDEM V3 raster data we used that was before the flood disaster on August 11, 2021, the flood events; in the 1st and 2nd regions, which are especially high risk, were checked from the news sources. Photographs showing the condition of the 1st and 2nd regions at the time of the flood are shown in Figure 13.

4.2. Calculation and Interpretation of Morphometric Parameters

4.2.1. Linear Morphometry

The basis of the linear morphometric features of the basin is the number and length of the stream sequences.

As shown in Figure 10, the number of indexes of the river network of the Ayancık Basin is 5, and by converting the raster data into vector data, it is possible to query the stream indexes as polylines. The length (Lu) and Frequency values (Fs) of the Ayancık Basin river sequences are shown in Table 3.

Figure 13. Photos showing the situation of the 1st and 2nd regions during the flood on August 11, 2021, in the Ayancık district. a-c-h [15], b [16], d [17], e[18], f [19], g [20], I [21]

Table 3. Ayancık Basin's Length of Stream Orders and Count of Stream Orders

Ayancık Basin		
Stream Orders	**Length of Stream Orders (km)**	**Count of Stream Orders**
1. Stream Order	160	95
2. Stream Order	73	34
3. Stream Order	71	42
4. Stream Order	23	14
5. Stream Order	5	4
Total	332	189

4.2.1.1. Mean Stream Length (Lsm)

The mean stream length (Lsm) shows the relationship of the drainage network with the relevant ground surface for each index; It is found by dividing the total stream length of the sequence by the number of streams. The formula for the Mean Stream Length is given in Table 2 and the results for each index are given in Table 4.

Table 4. Mean Stream Length of Stream Orders

Ayancık Basin	
Stream Orders	**Mean stream length of a given order**
1. Stream Order	1.684210526
2. Stream Order	2.147058824
3. Stream Order	1.69047619
4. Stream Order	1.642857143
5. Stream Order	1.25

4.2.1.2. Stream Length Ratio (Rl)

The Stream Length Ratio helps us to analyze whether the lengths of the lower tributaries are sufficient to carry the water coming from the upper tributaries to the stream's lower tributaries which are calculated as the ratio of the mean stream length of a given order to the mean stream length of next lower order.

Table 5. Stream Length Ratio (Rl) of Stream Orders

Ayancık Basin	
Stream Orders	Stream Length Ratio (Rl)
1. Stream Order	-
2. Stream Order	1.274816176
3. Stream Order	0.787345075
4. Stream Order	0.971830986
5. Stream Order	0.760869565

The ratio of the stream index of the 4th stream index is higher than the length ratio of the 5th stream index and the 3rd stream index (Table 5). This situation shows us that the waters accumulating in the 4th Stream index will collect in the 3rd and 5th Stream indexes due to reasons such as heavy rain and that the length of the 3rd and 5th Stream indexes will be insufficient and therefore will cause a flood disaster.

In the flood disaster on August 11, 2021, the bud storage area of the General Directorate of Forestry, located in the region where the 4th Stream index shown on the Stream Order Map in Figure 10, was mixed with the flood and to the 5th Stream index (district) as shown in the photographs in Figure 13. It was observed that it drifted towards the Babaçay village in the center of the river) and the 3rd stream index.

4.2.1.3. Bifurcation Ratio (Rb)

Bifurcation ratio (Rb), which explains the relationship of precipitation occurring in the basin with vegetation surface permeability and topography according to High and Low values; is calculated as the ratio of the number of stream segments present in the given order to the number of segments of the next higher order. The Bifurcation Ratio formula is shown in Table 2 and the calculated bifurcation rates for each index in the study are shown in Table 6.

Table 6. Bifurcation Ratio (Rb) of Stream Orders

Ayancık Basin		
Stream Orders	**Count of Stream Orders**	**Bifurcation Ratio (Rb)**
1. Stream Order	95	2.794117647
2. Stream Order	34	0.80952381
3. Stream Order	42	3
4. Stream Order	14	3.5
5. Stream Order	4	-

Basins with low Rb value have low permeability capacity, high runoff as well as higher and sharper flow hydrograph features. On the other hand, in basins with a high Rb value, it exhibits a hydrograph character with a high rate of infiltration and a less continuous flow. ([4], [12], [14]) In addition, the geology of the basins with an Rb value between 3-5, in general, has a more homogeneous structure [12].

It can be said that the geology of the basin has a homogeneous structure, since the bifurcation ratio values of the stream sequences of the Ayancık basin are between 3-5.

4.2.2. Relief Morphometry

Relief Morphometry is the analysis made with the slope and height values of the basins.

4.2.2.1 Basin Relief (Bh)

Basin relief, which is defined as the vertical distance between the highest value of the basin and the lowest elevation value, is a hydrological parameter. As can be seen on the DEM map shown in Figure 8, the highest elevation value of the Ayancık Basin is 1869.2 m and the lowest elevation value is 10.7 m. The perpendicular distance between these two points, Bh, is 1858.5 m.

4.2.2.2 Relief Ratio (Rh)

The Relief Ratio, which is calculated as the ratio of the vertical distance between the maximum and minimum basin height to the maximum basin length parallel to the mainstream, gives information about the drainage density and slope characteristics of the basin. The formula for Relief Ratio is shown on the map in Figure 14 with the maximum and minimum height values and the maximum basin length in Table 2. Ayancık Basin Relief Ratio (Rh) is 0.0138173.

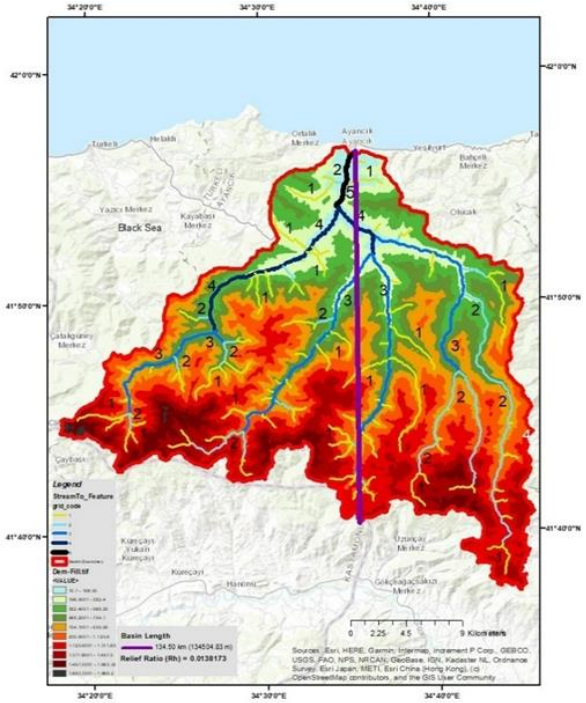

Figure 14. Relief Ratio and Basin Length map

4.2.2.3 Hypsometric Curve (Hc) and Integral (Hi)

The hypsometric curve shows the relationship between the ratio of the basin relative height to the total height and the ratio of the Relative area to the total area; It gives information about the erosion of the drainage network and the structure of the basin. The hypsometric integral is found by dividing the average height value of the basin from the minimum height value to the Basin relief and it shows the area under the hypsometric curve (Table 7). Relative height and relative area values of Hypsometric curve parameters are given respectively in Table 8 and in Figure 15.

Table 7. Hypsometric integral

Ayancık Basin		
Maximum Height	**Minimum Height**	**Average Height**
1869.00	10.00	889.00
Hi	0.47283	

Table 8. Hypsometric curve parameters

Relative Height (h)	Total Height (H)	Relative Area (a)	Total Area (A)	h/H	a/A
10.00	1869.00	674.05	674.05	0.01	1.00
197.00	1869.00	650.90	674.05	0.11	0.97
382.00	1869.00	596.83	674.05	0.20	0.89
568.00	1869.00	518.43	674.05	0.30	0.77
754.00	1869.00	425.03	674.05	0.40	0.63
939.00	1869.00	318.28	674.05	0.50	0.47
1126.00	1869.00	206.86	674.05	0.60	0.31
1312.00	1869.00	102.49	674.05	0.70	0.15
1498.00	1869.00	29.25	674.05	0.80	0.04
1683.00	1869.00	2.12	674.05	0.90	0.00
1869.00	1869.00	0.00	674.05	1.00	0.00

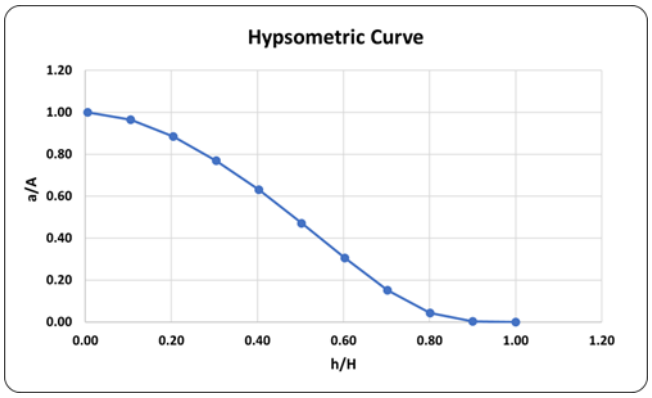

Figure 15. Hypsometric curve (Hc)

Hypsometric integral value and hypsometric curve plot; It shows that the erosion cycle of the Ayancık Basin is between the Young - Mature phase, in other words, the erosion phase is in a trend close to maturity.

4.2.2.4. Ruggedness Number (Rn)

The roughness value of the Basin, calculated by the product of Basin Relief and Drainage Density, gives information about the surface flow and erosion of the basin. The rate of flooding is higher in basins with a high Rh ratio. The Basin Relief Value of the Ayancık Basin is 1858.5m and the Drainage Density Value is 0.492545 (km/km^2). In order to calculate the roughness ratio, the formula which is shown in Table 2, Basin Relief was first converted from m units to km units. The Roughness value of the Ayancık Stream Basin is 0.91539.

4.2.3. Areal Morphometry

Areal Morphometry is the analysis of the basin with area and length information.

4.2.3.1. Drainage Density (Dd)

Drainage Density (Dd), which has a positive relationship with Flood and Flood events; is found by the ratio of the total river length to the basin area. The formula in Table 2 and the total stream index length in Table 3 are shown. The area of the Ayancık Stream basin is 674.05 km^2, and the drainage density is 0.492545 (km/km^2). This value shows that the surface waters infiltrate underground in the Ayancık stream basin and the river intervals are wide.

4.2.3.2. Stream Frequency (Fs)

Stream Frequency value is calculated by the ratio of the total number of stream indexes to the catchment area; if it is high, it indicates non-permeable soil properties and high relief values, if low, and it indicates permeable geological properties and low relief properties. The total number of stream indexes is shown in Table 3 and the Stream Frequency formula is shown in Table 2. The stream frequency (Fs) of the Ayancık Basin is 0.280394.

4.2.3.3. Texture Ratio (T)

Texture Ratio (T), which is calculated by the ratio of the total length of the first stream index obtained by the Strahler method to the perimeter of the basin shows a high value in circular basins and a low value in longitudinal basins. The total length of the 1st stream sequence of the Ayancık stream basin is shown in Table 3, and the Texture Ratio formula is shown in Table 2. The circumference of the basin is 161.33 km. The Texture Ratio value of the Ayancık stream basin is 0.99175.

4.2.3.4. Form Factor (Rf)

Form Factor is calculated by the ratio of the basin area to the square of the maximum basin length and gives information about the circularity of the basin. The formula is shown in Table 2. The Form Factor (Rf) value of the Ayancık basin is 5.0115.

4.2.3.5. Circulatory Ratio (Rc)

Circularity ratio; It is calculated by multiplying the basin area (A) by 4π and dividing by the square of the basin perimeter (P). The closer the value is to 1, the greater the circularity [10]. The circularity map is shown in Figure 16.

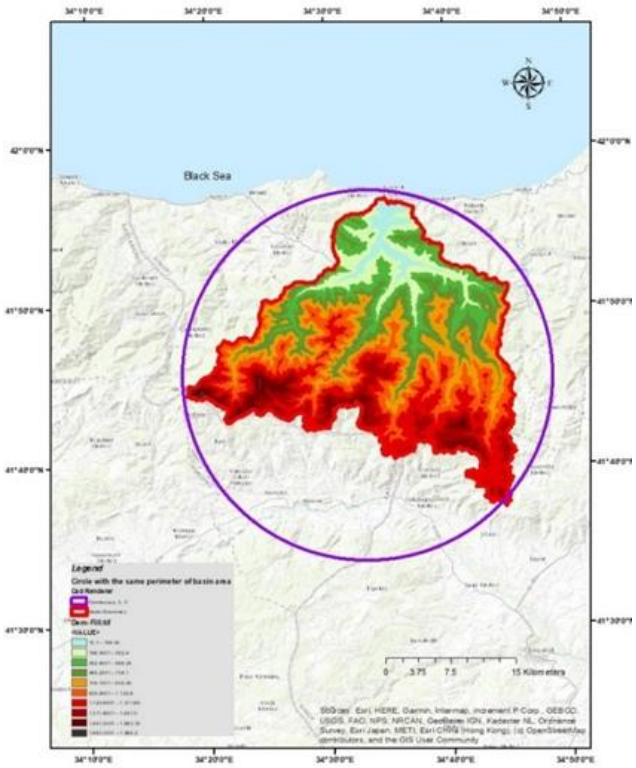

Figure 16. Circulatory Ratio (Rc) Map

The Texture Ratio, Form Factor, and Circulatory Ratio results support each other and show that the Ayancık Stream basin is a basin with circular characteristics.

4.2.3.6. Elongation Ratio (Re)

Elongation Ratio (Re), which is obtained by the ratio of the diameter of a circle with the same area as the basin to the maximum length of the basin, gives information about the infiltration capacity and surface flow of the basin. Ayancık Stream Basin area is 674.05 km2 and the diameter of a circle with the same area as the basin is found from the formula πr^2. The combined version of the formula is shown in Table 2. The Length Ratio of the Ayancık Stream Basin is 0.108969.

4.2.3.6. Length of Overland Flow (Lg)

Length of Overland Flow, which expresses the length of the water on the ground surface before it reaches the flow channel; it is inversely proportional to Drainage Density. Its formula is given in Table 2. The Length of the Overland Flow value of the Ayancık Stream Basin is 0.98509.

4.2.3.7. Constant Channel Maintenance (C)

It is a constant used to determine how many square kilometers of surface area in the basin is required to form a linear foot of the stream channel. The formula is given in Table 2.

A surface area of 2.03 km^2 is required in the basin required for the formation of a linear foot of the Ayancık Stream channel. The C constant of the Ayancık Stream basin is 2.03 km^2.

5. Discussion

The hypsometric curve graph and the integral value showed that the erosion cycle of the Ayancık Basin is in a trend from young to maturity. Since the river valleys show erosion up to the sea level during the maturity stage of the rivers, it is recommended to determine and evaluate the flow and erosion data of the Ayancık Stream over the years while determining the elevation in the creek improvement studies carried out and/or to be made in the region.

Since the Stream Density map obtained was found to be exactly compatible with the areas most affected by the flood disaster that occurred in the Ayancık district on August 11, 2021, it is recommended to perform a flood analysis in the region and to analyze the change in the topography over the years. When the region is examined, it is suggested that settlement maps should be prepared to prevent loss of life and property in case of a possible flood or flood, since the roughness of the land is high.

6. Conclusion

In this study, the boundary and morphometric features of the Ayancık Stream basin were determined by using remote sensing and GIS. In the Stream Density map obtained with the indexes in the drainage networks, areas with a high probability of flooding and flooding were determined. It has been concluded that among these regions, especially the 1st and 2nd Regions are the same as the areas most damaged in the flood disaster on 11 August 2021. For this reason, it has been concluded that these regions are areas where precautions should be taken first.

According to the morphometric characteristics of the basin; Roughness Ratio and Basin relief, it is seen that the basin area has steep slopes and a valley-shaped stream bed is formed. This result supports the difference between the maximum and minimum height in the DEM data.

It has been concluded that the erosional phase of the basin is in a tendency close to maturity and has the characteristic of a circular basin. As a result, it was concluded that there is a flood risk in the Ayancık Stream Basin. The basin model analysis and morphometric parameters obtained as a result of this study have been determined to be a base for flood and flood risk analyses and management plans.

Author contributions

Emine Müjgan ERGENE: Data download, Image processing, calculation, analysis and interpretation, Methodology, Writing, Visualization **Elnaz NAJATISHENDI:** Data curation, Image processing, Software, Validation. **Füsun Balık ŞANLI and Anime Melis Uzar DİNLEMEK:** Investigation, Writing-Reviewing and Editing.

Conflicts of interest

The authors declare no conflicts of interest.

References

1. http://global-flood-database.cloudtostreet.ai/
2. https://www.afad.gov.tr/kurumsal-raporlar
3. Horton, R. E. (1945). Erosional Development of Streams and Their Drainage Basins; Hydrophysical Approach to Quantitative Morphology. Geological Society of America Bulletin, 56, 275.
4. Strahler, A. N. (1964). Quantitative geomorphology of the drainage basin and channel networks, Handbook of applied hydrology.
5. Schumm, S. A. (1956). Evolution of drainage systems and slopes in badlands at Perth Amboy. New Jersey, Geological society of America bulletin, 67, 597-646.
6. Miller, V. C. (1953). A Quantitative geomorphic study of drainage basin characteristics in the Clinch Mountain area Virginia and Tennessee.
7. Smith, K. G. (1950). Standards for grading texture of erosional topography. American Journal of Science, 248, 655–668.
8. Strahler, A. N. (1952). Hypsometric (Area altitude) analysis of erosional topology. Geological Society of America Bulletin, 63(11), 1117-1142
9. Strahler, A. N. (1958). Dimensional analysis applied to fluvial eroded landforms. Geological Society of America Bulletin, 69, 279-300
10. Ödeker B. & Türkoğlu N. (2020). Sabuncular Deresi Havzası'nın (Rize/Çayeli) Morfometrik Özelliklerinin Coğrafi Bilgi Sistemleri (CBS) İle Belirlenmesi, DTCF Dergisi 60.1: 14-38, DOI: 10.33171/dtcfjournal.2020.60.1.2
11. https://asterweb.jpl.nasa.gov/GDEM.asp
Date of access: 23 April 2022
12. Özdemir, H. (2011) Havza Morfometrisi ve Taşkınlar. Fiziki Coğrafya Araştırmaları, Sistematik ve Bölgesel, Türk Coğrafya Kurumu Yayınları. 507-526
13. Görgülü, E., Göl, C., (2021). Coğrafi Bilgi Sistemleri ile havza morfometrik analizi: Sarayköy Göleti Havzası (Çankırı). Anadolu Orman Araştırmaları Dergisi, 7(2), 107-118
14. Utlu M., Özdemir H. (2018) Havza Morfometrik Özelliklerinin Taşkın Üretmedeki Rolü Biga Çayı Havzası Örneği, Coğrafya Dergisi – Journal of Geography 36, 49-62. DOI: 10.26650/JGEOG408101
15. https://www.haberturk.com/son-dakika-sinop-ta-sel-felaketi-sinop-ayancik-sel-felaketinde-son-durum-3159719 Date of access: 23 April 2022
16. https://www.pusulahaber.com.tr/sinopta-sel-ayancik-cayi-tasti-1450223h.htm Date of access: 23 April 2022
17. https://m.bianet.org/bianet/iklim-krizi/248746-ayancik-dag-koylerinde-tahribat-cok-buyuk Date of access: 23 April 2022
18. https://www.aa.com.tr/tr/gundem/ayancikta-sel-sularinin-altyapi-ve-dogaya-tahribati-havadan-goruntulendi/2365192 Date of access: 23 April 2022
19. https://www.eskisehirhaber.com/asayis/sinop-ayanciktaki-sel-afeti-havadan-goruntulendi-h474127.html Date of access: 23 April 2022
20. https://www.dunya.com/gundem/bartin-kastamonu-ve-sinopta-sel-felaketi-6-olu-1-kayip-haberi-630513 Date of access: 23 April 2022
21. https://www.sozcu.com.tr/2021/gundem/sinopta-sel-ayancik-cayi-tasti-6586692/

Mersin Photogrammetry Journal
https://dergipark.org.tr/en/pub/mephoj
e-ISSN 2687-654X

Production of flood risk maps: Ayancık Stream Example

Elnaz Najatishendi*[1], Emine Müjgan Ergene[1], Melis Uzar[1], Füsun Balık Şanlı[1]

[1]*Yildiz Technical University, Department of Geomatics Engineering, Türkiye*

Keywords
Remote sensing
photogrammetry
Flood
Risk maps
GIS

Research Article
DOI:10.53093/mephoj.1123378

Received: 30.05.2022
Accepted: 06.07.2022

Abstract

Natural disasters are events that negatively affect human life and cause material and moral damages. As in the rest of the world, one of the biggest natural disasters after earthquakes in our country is floods. The flood event turns into a disaster in cases caused by human interventions such as the change of the river bed, the increase in the construction on the riversides, and the blocking of the river perpendicular to the flow direction. In this study, risk maps for floods with different return intervals (25, 50, 100 years) were produced with GIS for Ayancık stream in Sinop province. As a result, when the flood risk maps were analyzed, the regions located in the floodplain were considered very risky regions. According to the results obtained, the flood disaster reaches a depth of 7 meters. Ayancık Stream and its surroundings are a very risky area exposed to floods as they have a maximum depth of 3.5 m. In addition, flood risk areas with 50 and 100-year return period floods, increase 3.71 and 12.83 percent, respectively, from 25-year return period flood risk areas.In addition, it was concluded that the majority of the areas affected by the floods in all three turning ranges within the scope of the study area are located in the very risky region, while the extreme risk areas are less than the other risky groups.

1. Introduction

Natural or human-induced events that cause life, economic and social losses for people and cause interruption of public life and human activities for a certain period of time are defined as “disaster” [1]. Many countries, depending on its geography, climatic conditions, and geological and topographical features, are exposed to meteorological natural disasters that result in significant loss of life and property from time to time. One of these natural disasters is flooding.

Floods are one of the natural disasters that cause significant loss of life and property in our country and many parts of the world. Major floods in Turkey are a combination of regional climate, topography and basin area factors. As we move inlands from the seas on our north, west and south coasts, the humidity in the atmosphere decreases. Heavy rains and large floods occur in high elevation areas perpendicular to the humid air flow, such as on the Black Sea and Mediterranean coasts. Floods in large basins areas are formed by the accumulation of rain as well as melting snow, but in small basins are mainly caused by rainfall [2].

Although the main factor of flood events is known as precipitation, the destruction of the natural features of the river basins day by day, the intense use of land and the wrong interventions on the river beds cause even the normal precipitation for the basin and river beds to cause floods. In addition, engineering structures built on rivers sometimes lead to the evaluation of features that did not pose a risk before as a risk. This causes some new plans to be considered in risk management studies for land uses near the river bed [3].

Risk management, which is a systematic process, consists of risk identification, risk analysis and determination of the amount of risk. Efforts to minimize the loss of life and property in a possible flood and to reduce the harmful effects of the flood can be carried out with risk management in flood areas.

In risk management studies; hazards and risks are determined, risk scenarios are prepared, protection and mitigation measures are selected, the results are

* **Corresponding Author**

*(elnaz.najatishendi@std.yildiz.edu.tr) ORCID ID 0000-0001-7901-5640
(mujganergene@gmail.com) ORCID ID 0000-0002-1118-0006
(auzar@yildiz.edu.tr) ORCID ID 0000-0003-0873-3797
(fbaliksanli@gmail.com) ORCID ID 0000-0003-1243-8299

Cite this article

Najatishendi, E., Ergene, E. M., Uzar, M., & Şanlı, F. B. (2022). Production of flood risk maps: Ayancık Stream Example. *Mersin Photogrammetry Journal, 4(1), 24-31*

presented with current maps and graphics, resources and opportunities that can be used are determined, and decisions about the most appropriate options and priorities for disaster protection and disaster response are eliminated and implemented [4].

Various methods and tools have been developed within the scope of flood risk management in the world. One of the most important of these tools is geographic information systems. The use of GIS, especially in the analysis of risk scenarios, is increasing day by day because the use of remote sensing and GIS technologies together in wide geography makes this tool attractive. Desalegn et al. [5] used GIS and HEC-RAS model for mapping flood inundation areas at Fetam River, Upper Abbay Basin, Ethiopia. As a result, they obtained flooded areas along the side of the Fetam River are 27.31, 24.85, 20.47, 17.34, and 13.78 km2 for 100, 50, 25, 10, and 5 years return periods, respectively. Moreover, Losub et al. [6] performed flood risk maps analyses in northern part of the Neamt county, North-Eastern region, Romania by using HEC-RAS method with the HEC-GeoRAS. As a result, they determined the correlation with the field situation and flood risk in a very high proportion. According to the simulation; for a 1% occurrence flood, almost 123 damaged households and a number of 147 damaged buildings have been detected.

In the study area, urbanization was established around the Ayancık stream. For this reason, it is foreseen that the first area to be affected in the event of a flood will be the district center where urbanization is located. Our aim in this study is to scientifically prove that the city center located around the Ayancık stream is at risk of flooding, and thus to determine the areas where precautions should be taken.

In this study, the production and evaluation of risk maps were carried out with the integration of remote sensing and GIS. Precipitation, soil, land use, and digital terrain model were used at this stage. As a result, flood risk areas were determined for the Ayancik region, and their impact on settlement areas was evaluated.

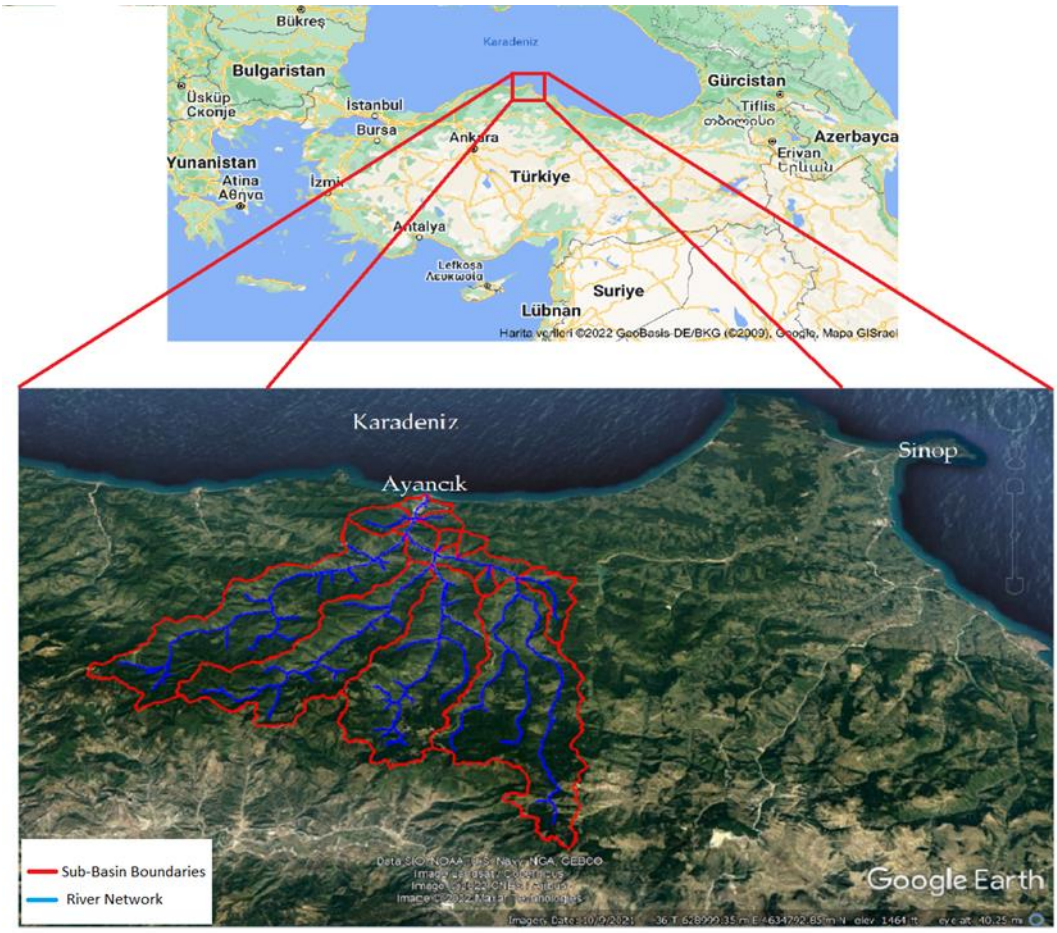

Figure 1. Ayancık stream precipitation basin settlement map

2. Study area and data used

Ayancık Stream is located in the Black Sea region and is connected to the province of Sinop. It is located at a distance of 47 kilometres from the province of Sinop and at a latitude of 41.9484 and a longitude of 34.5931 (Figure 1). In Figure 1, the Ayancık Stream basin and its sub-basins are shown with red lines, and Ayancık Stream networks are shown with blue lines. The basin area is 676.54 km^2 and the average height of the basin is 884.14 m, and it is a river pouring into the Black Sea. Ayancık region has a typical Black Sea climate, with cool and rainy winters and dry and humid summers. The annual average temperature is 14.0 C degrees. The highest

average temperature is 22.2 °C in July, and the lowest average temperature is 6.6 °C in January-February. The annual average relative humidity is 72%, the humidity reaches its highest value at 76% in March, and its lowest value at 70% in June, July and December.

The annual average precipitation is 676 kg/m ^{2}, the highest precipitation is in December with 139.2 mm, and the lowest is in July with 34.9 mm. Its high parts are usually covered with snow during the winter season. Forests form the natural vegetation of the region. The vegetation is very rich and dense and differs according to the altitude zones. In the coastal part, broad-leaved forest texture, maquis and heaths and cultivated plants are common. As it rises from the coast, coniferous tree and plant species gain density. There are pine, fir, oak, hornbeam, beech, ash, elm, linden, plane tree, chestnut, poplar and various maquis and shrub species in the forests [7].

2.1. Numeric Elevation Data

ASTER (Advanced Spaceborne Thermal Emission and Reflection Radiometer) is generally preferred in the creation of Digital Elevation Models (DEM) due to the advantage of having wider coverage and better temporal and spatial resolution [8]. The resolution of the DEM data used in this study is 6.7 m. DEM maps of the Ayancık Stream basin are given in Figure . ASTER global SYM (ASTER Global Digital Elevation Map – GDEM) has been published as the product of a joint project between the Japanese Ministry of Economy, Trade and Industry (METI) and the United States Aerospace Administration (NASA). The first version of the ASTER GDEM model was presented to users in June 2009. In the calculation of the model, it was obtained by evaluating the stereo-dual satellite images obtained from the ASTER (Advanced Spaceborne Thermal Emission and Reflection Radiometer) sensor on the Terra satellite of the NASA Earth Observing System (Eath Observing System-EOS) [9]. The quality and accuracy of ASTER GDEM global SYM versions are evaluated and reported by the ASTER evaluation working group, with 20 members led by the United States and Japan [10]. The ASTER GDEM V3 maintains the GeoTIFF format and the same gridding and tile structure as V1 and V2, with 30-meter postings and 1 x 1-degree tiles [11].

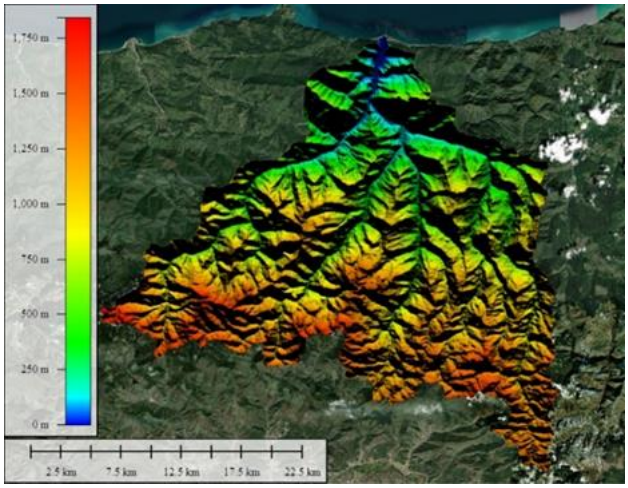

Figure 2. DEM maps of the Ayancık Stream basin

2.2. Precipitation Data

In this study, rain intensity values were obtained from rainfall intensity (i), rainfall duration (t) and recurrence time(T)(i-t-T) curves (Figure 3) of the Sinop meteorological observation station operated by the General Directorate of Meteorology (MGM). In addition, the precipitation values used with 25, 50 and 100 year return intervals and 24-hour periods, respectively, are given in Table 1 (In this study, rainfall values were obtained from the i-t-T curves (Figure 3) of the Sinop Meteorological Observatory, which operated by the General Meteorological Office (MGM). İn addition, the rainfall values used with return intervals of 25, 50 and 100 years and 24-hour periods, are given respectively in Table 1.

Table 1. Frequency analysis of 24-hour precipitation in Sinop station [13]

Recurrence Period (Year)	Precipitation (mm/hour)
25	4.5
50	5.5
100	6.5

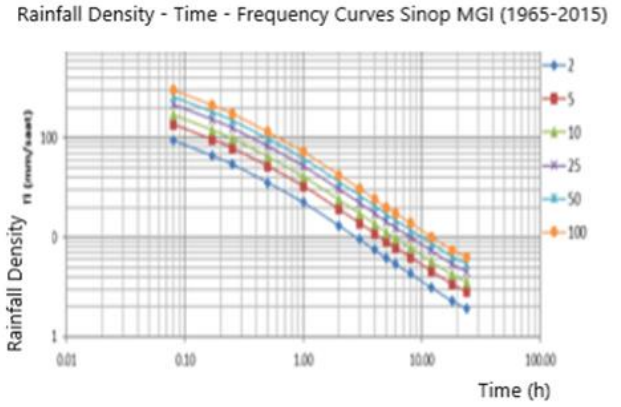

Figure 3. Sinop MGI i-t-T curves

2.3. Land Cover Map

Land cover maps were obtained from geophysical parameters derived from next-generation satellite images within the scope of the European Space Agency (ESA) Climate Change Initiative (CCI) projects (Figure 4).

These maps were prepared as a global land cover map with 300 m spatial resolution on an annual basis from 2016 to 2019, consistent with the global annual LC maps series from 1992 to 2015. The maps in netcdf format (2016 - 2019) were downloaded via the Copernicus Climate Change Service (C3S) Climate Data Store (CDS). In addition, C3S is implemented by the European Center for Medium-Range Weather Forecasts (ECMWF) on behalf of the European Commission [12].

2.4. Soil Type Map

The Harmonized World Soil Database is a 2-degree grid with over 15,000 different soil mapping units combining information contained in current regional and national soil information updates (SOTER, ESD, oil Map of China, WISE) worldwide. raster database. This

database includes the 1: 5 000 000 scale FAO-UNESCO World Soil Map (FAO, 1971-1981). As shown in Figure , the study area consisted of soil types B (Loam) and C (sandy clay loam).

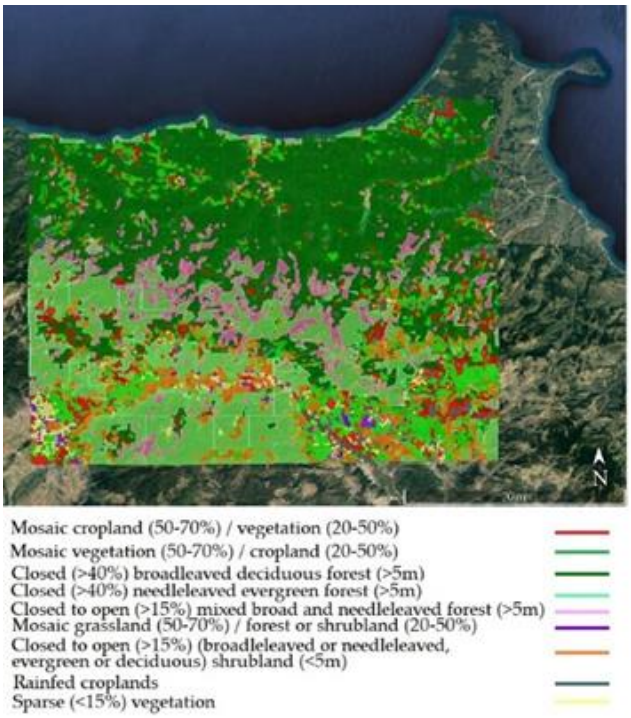

Figure 4. Ayancık basin land use map (ESA)

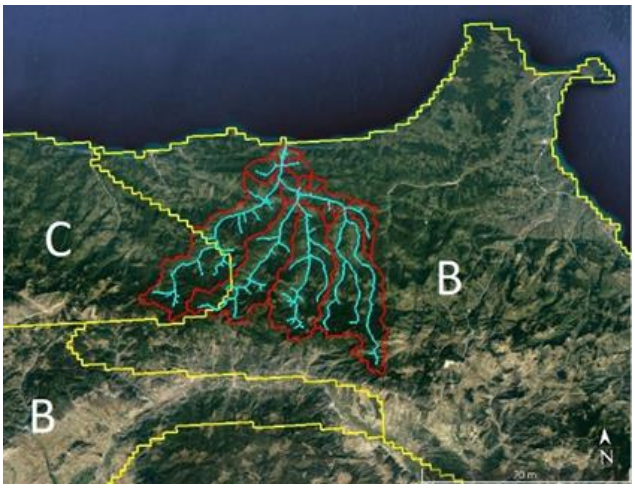

Figure 5. Soil type map of the study area

3. Methodology

A workflow chart is given to produce flood risk maps (Figure 6).

In the first stage for the production of flood risk maps, Digital Elevation Model (DEM), land use map, soil type map, and precipitation-intensity-recurrence curve of the study area were obtained to be used in hydrological and hydraulic models. In the second stage, Flood Hydrographs with various rotation intervals were obtained with the help of HEC HMS software using GIS data and Precipitation-Intensity-Recurrence curves (with The Soil Conservation Service (SCS) Curve Number (CN).

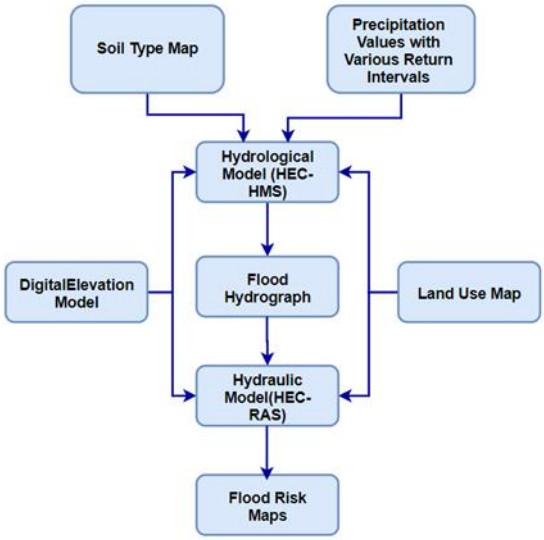

Figure 6. Workflow diagram for flood risk maps

The SCS CN method, also known as the flow curve number method, is a method developed by the Agricultural Soil Conservation Service of America, which estimates precipitation excess (direct flow).

$$S = (1.000 / CN) - 10 \text{ (mm)} \quad (1)$$

$$Q = (P - 0.2S)2/(P+0.8S) \quad (2)$$

The CN curve number is obtained from the SCS table (Table 2) and the S value is calculated from the equation. In this equation, P is the precipitation amount in mm and Q is the flow rate (m^3/s).

In the third stage, flood risk maps (HEC-RAS) consisting of precipitation values with 25, 50, and 100 year return intervals and 24-hour duration were obtained.

4. Results

Flood risk maps have been created for Ayancık Stream. After the precipitation data with various return intervals were obtained from the Precipitation-Intensity-Recurrence curves, flood hydrographs were obtained from the SCS curve number obtained from the land cover and soil type maps. Flood maps were obtained by creating a hydraulic model with these hydrographs. As a result, these maps were analyzed and evaluated in the GIS environment of the data obtained by remote sensing and photogrammetry, and risk classification based on depth was made.

4.1. Classification of Flood Risk Areas

Flood areas are classified according to the three critical depths of 0.6, 1.0, and 3.5m. For selecting critical depths, the height of school and public buildings from the ground is 0.6 m. If the flood depth is more than 1.0 m, there is a possibility of a loss of life. In addition, major damage is expected in agricultural production. The minimum threshold height for shelters and one-story buildings is usually 3.5 m. Hazard classification according to flood depth is given in Table 3.

Table 2. SCS Curve Number Table [14]

Land Use Description on Input Screen	**Description and Curve Numbers from TR-55** **Cover Description** Cover Type and Hydrologic Condition	% Impervious Areas	**Curve Number for Hydrologic Soil Group** A	B	C	D
Agricultural	Row Crops - Straight Rows + Crop Residue Cover-Good Condition		64	75	82	85
commercial	Urban Districts: Commercial and Business	85	89	92	94	95
forest	Woods - Good Condition		30	55	70	77
Grass/ Pasture	Pasture, Grassland, or Range [3] - Good Condition		39	61	74	80
High-Density Residential	Residential districts by average lot size: 1/8 acre or less	65	77	85	90	92
industrial	Urban district: Industrial	72	81	88	91	93
Low-Density Residential	Residential districts by average lot size: ½ acre lot	25	54	70	80	85
Open Spaces	Open Space (lawns, parks, golf courses, cemeteries, etc.) [4] Fair Condition (grass cover 50% to 70%)		49	69	79	84
Parking and Paved Spaces	Impervious areas: Paved parking lots, roofs, driveways, etc. (excluding right-of-way)	one hundred	98	98	98	98
Residential 1/8 acre	Residential districts by average lot size: 1/8 acre or less	65	77	85	90	92
Residential 1/4 acre	Residential districts by average lot size: 1/4 acre	38	61	75	83	87
Residential 1/3 acre	Residential districts by average lot size: 1/3 acre	30	57	72	81	86
Residential 1/2 acre	Residential districts by average lot size: 1/2 acre	25	54	70	80	85
Residential 1 acre	Residential districts by average lot size: 1 acre	20	51	68	79	84
Residential 2 acres	Residential districts by average lot size: 2 acres	12	46	65	77	82
Water / Wetlands		0	0	0	0	0

Table 3. Type of flood risk [15]

Flood hazard no.	Flood depth, d, (m)	Type of flood hazard
T1	0<d<0.6	Little
T2	0.6<d<1.0	Middle
T3	1.0<d<3.5	A lot
T4	3.5<d	Extreme

4.2. Flood Hydrographs (HEC –HMS Model)

HEC-HMS software was used for hydrological analysis. This basin was divided into 10 sub-basins and the SCS method was applied. For this method, the curve numbers of the sub-basins were used from soil type and ground cover maps.

Ayancık basin was divided into ten sub-basins and 24-hour flood hydrographs were obtained for precipitation values at various return intervals for each sub-basin. These hydrographs are shown in Figures 7-9.

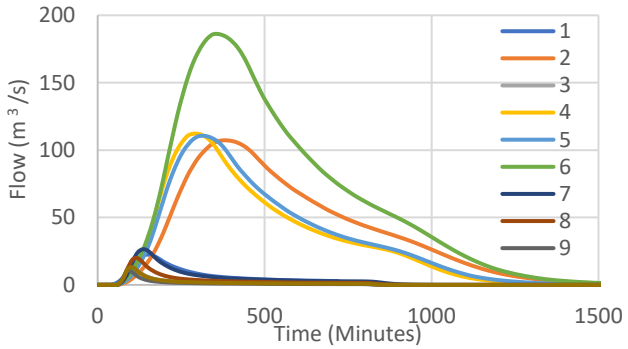

Figure 7. Flood hydrograph of Ayancık Stream sub-basins with 25-year return interval.

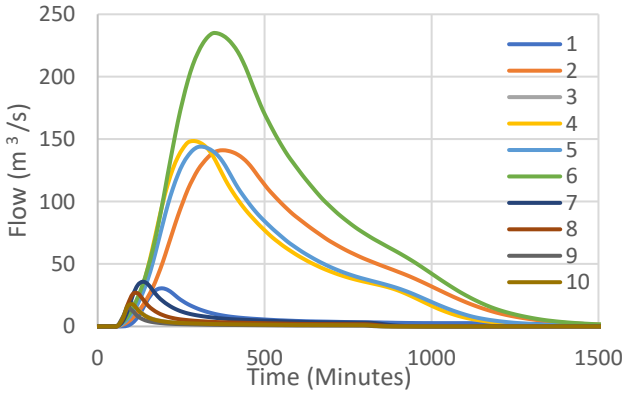

Figure 8. Flood hydrograph of Ayancık Stream sub-basins with 50-year return interval

4.3. Flood Maps (HEC-RAS Model)

In this study, HEC-RAS software was used to obtain flood maps. The prepared digital calculation mesh (10×10 m resolution) is shown in Figure 10. The boundaries of the floodplain were determined, as shown in Figure 10. In addition, the boundaries of discharges to the main bed of each sub-basin (10 sub-basins) are shown in the Figure 10.

As a result of 24-hour model studies, results were obtained for all three return intervals (25, 50, and 100 years), and flood spread maps are shown in Figures 11, 12, and 13. The area affected by each intermittent return flood was obtained and is given in Table 3. As shown in Figures 11, 12, and 13, the maximum water depth is 7 m. A combined view is given in Figure 14 to compare the flood risk maps generated by the modeled precipitations with various return intervals. According to the topographic condition of the creek, the area exposed to flooding is close in all three scenarios (Table 4). In this distribution map, the area shown in red represents the flood area with a 25-year return interval, the area shown in blue is the flood area with a 50-year return interval, and the green is the flood area with a 100-year return interval.

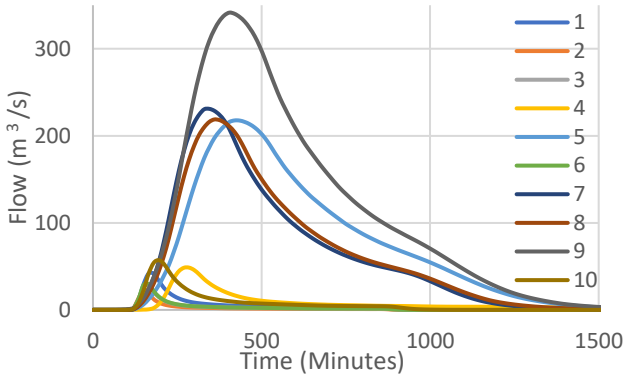

Figure 9. Flood hydrograph of Ayancık Stream sub-basins with 100-year return interval

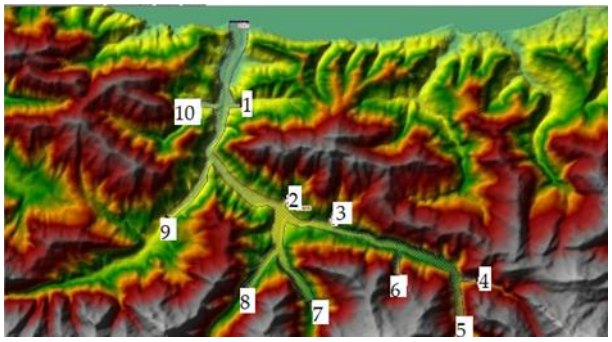

Figure 10. HEC-RAS model numerical computational network image and location of borders

Table 4. Flood maps obtained as a result of various return ranges

Return range (year)	Area (km ²)
25	3.178
50	3.296
100	3.586

5. Conclusion

Ayancık Stream is an important study area due to its regional and climatic characteristics. In this study, three scenarios, for 25, 50, and 100 year intermittent rain, were considered. The flooded areas are divided into three critical depths of 0.6, 1.0, and 3.5 m. Accordingly, 0-0.6 m deeplow-riskk zone, 0.5-1.0 m deep medium risk zone, 1.0-3.5 m deep high-,risk zone and more than 3.5 m depth extreme risk zone are classified into four groups.

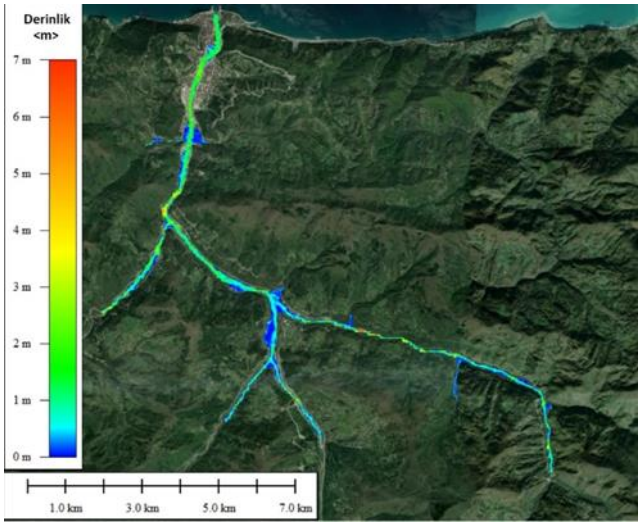

Figure 11. Ayancık creek flood spread map with 25-year return interval

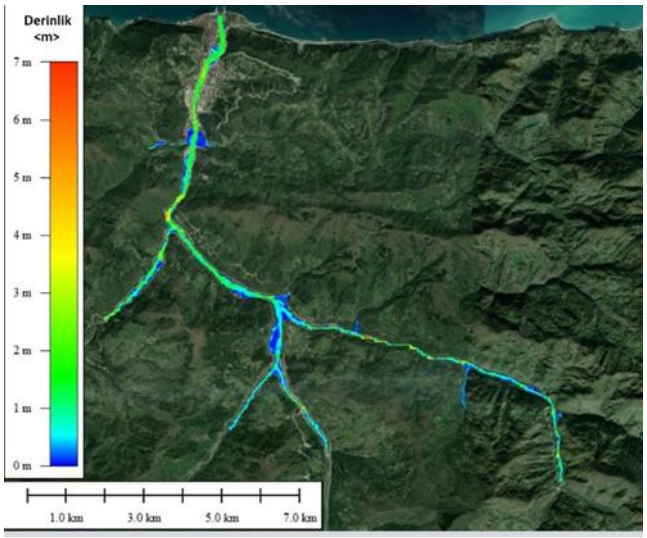

Figure 12. Ayancık Stream flood spread map with 50-year return interval.

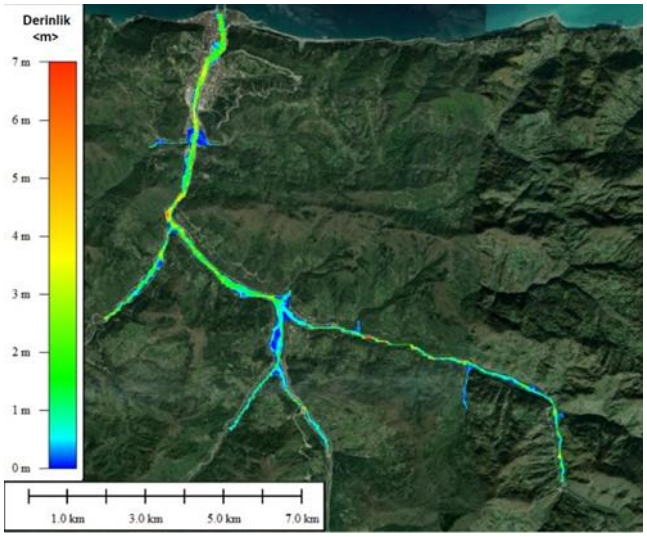

Figure 13. Ayancık creek flood spread map with a 100-year return interval

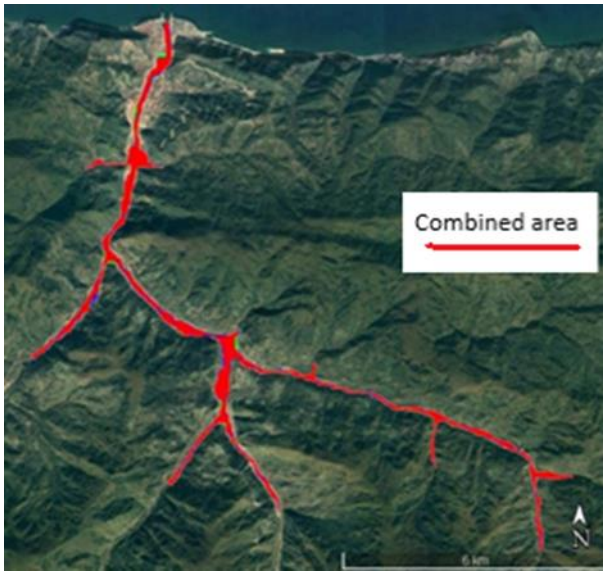

Figure 14. Combined view of risk maps.

In all 3 cases, the depth to which the flood will reach is 7 m, and most of the flood area is below the depth of 3.5 m. This shows that the floodplain of the creek will be located in a very risky region if precipitation with 25, 50, and 100 year return intervals occurs.

As a result of the analysis, it is suggested that urbanization should be controlled in areas close to the floodplain (in risky areas) so that the settlements located in the downstream region of the stream are not affected by the flood. An important result is that urbanization activities should not be allowed in cases of T1, T2, and T3 (flood hazard No.). In the current urbanization situation, information should be given to the civil and authorized administrations living in the region for urgent measures using advanced technology warning systems. Within the scope of disaster management, the rapid evacuation of all kinds of obstacles reduces the discharge capacity of the region and the stream, for example, the existing boats at the exit to the sea during floods. The academic and scientific solution proposal is to take measures according to the current situation analysis by considering the important criteria integrated with remote sensing and GIS and predicting future floods and accommodation, residence, etc., critical in areas close to flood risk areas. Floods are big threat in human life for communities and individuals that should not be allowed. As a result, with the increasing importance of such studies, the risk of flooding will be prevented in the future.

Author contributions

Emine Müjgan ERGENE: Data download, Image processing, calculation, analysis and interpretation, Methodology, Writing, Visualization **Elnaz NAJATISHENDI:** Data curation, Image processing, Software, Validation. **Füsun Balık ŞANLI** and Anime **Melis Uzar DİNLEMEK**: Investigation, Writing-Reviewing and Editing.

Conflicts of interest

The authors declare no conflicts of interest.

References

1.https://www.afad.gov.tr/kurumlar/afad.gov.tr/2419/files/Afet_Mud_Pl_ResmiG_20122013.pdf
2. Özalp, D. (2009). Dere Taşkın Risk Haritalarının CBS Kullanılarak Oluşturulması ve CBS İle Taşkın Risk Analizi, Doktora Tezi, Geomatik Mühendisliği, Fen Bilimleri Enstitüsü, İstanbul Teknik Üniversitesi, İstanbul.
3. Özdemir, H. (2007). Farklı Senaryolara Göre Taşkın Risk Analizi: Havran Çayı Örneği (Balıkesir). TMMOB Afet Sempozyumu, 5–7 Aralık 2007, Ankara.
4. Özcan Ö, Musaoğlu N & Şeker D Z (2009). Taşkın Alanlarının CBS ve Uzaktan Algılama Yardımıyla Belirlenmesi ve Risk Yöntemi: Sakarya Havzası Örneği. TMMOB Harita ve Kadastro Mühendisleri Odası 12. Türkiye Harita Bilimsel ve Teknik Kurultayı, 11 – 15 Mayıs 2009, Ankara.
5. Desalegn, H., & Mulu, A. (2021) Mapping flood inundation areas using GIS and HEC-RAS model at Fetam River, Upper Abbay Basin, Ethiopia. Scientific African
6. Iosub, M., Minea, I., Hapciuc, O., & Romanescu, Gh. (2015) The Use of Hec-Ras Modelling In Flood Risk Analysis, International Journal On Humanistic Ideology, 315-322
DOI: 10.17378/AWC2015_42
7. http://www.ayancik.gov.tr/cografi-yapisi
8. Eckert, S., Kellenberger, T., & Itten, K. (2004). Accuracy Assessment of Automatically Derived Digital Elevation Models from Aster Data in Mountainous Terrain: RSL-Remote Sensing Laboratories, Department of Geography, University of Zurich, CH-8057 Zurich, Switzerland.
9. Sümer, E. Ö., Gürçay, B., Pekesin, B. F., Avcı, K., Koruyucu, M., Dağlıyar, A., Teoman, A., Topçu, T. and Özgüner, C., 2006. ASTER Uydu Verisi Uygulamaları: Türkiye'den Örnekler. Özel Yayın Serisi-5, Maden Tetkik Arama Genel Müdürlüğü, 70, Ankara. ISBN: 975-8964-41-0.
10. Tachikawa, T., Kaku, M., Iwasaki, A., Gesch, D., Oimoen, M., Zhang, Z., Danielson, J., Krieger, T., Curtis, B., Haase, J., Abrams, M., Crippen, R. and Carabajal, C., 2011. ASTER Global Digital Elevation Model Version 2 – Summary of Validation Results. U.S., NASA Land Processes Distributed Active Archive Center 25.
11. URL 4: https://asterweb.jpl.nasa.gov/GDEM.asp
12.http://maps.elie.ucl.ac.be/CCI/viewer/download.php
13. Korkmaz, B., Şen, K., Aksu, H., (2019). Periodic precipitation-intensity and duration analysis for the Central Black Sea, Muğla Sıtkı Koçman University 10th National Hydrology Congress 9-12 October, 2019
14. Urban Hydrology for Small Watersheds United StatesDepartment of Agriculture, Natural Resources Conservation Service, Conservation Engineering Division Technical Release 55, June 1986
15. Tingsanchali, T., & Karim, M. F. (2005), Flood Hazard and Risk Analysis in the Southwest Region of Bangladesh, Hydrological Processes, 19, 2055-2069

Mersin Photogrammetry Journal

https://dergipark.org.tr/en/pub/mephoj

e-ISSN 2687-654X

Modelling Ozancık village (Aksaray) in computer environment using UAV photogrammetry

Hacı Murat Yılmaz*[1], Nusret Aktan[2], Adem Çolak [2], Aydın Alptekin [3]

[1]*Aksaray University, Geomatics Engineering Department, Türkiye*
[2]*Aksaray Special Provincial Administration, Aksaray, Türkiye*
[3]*Mersin University, Geological Engineering Department, Türkiye*

Keywords
Terrain modelling
UAV
DSM
Ortomosaic

Research Article
DOI:10.53093/mephoj.1132303

Received: 20.06.2022
Accepted: 04.07.2022

Abstract

Modelling the terrain with high accuracy is vital to create modern settlement areas, and to find solutions that threaten the people. Traditional land surveying is a time-consuming and expensive method. Unmanned aerial vehicle (UAV) is a powered aerial vehicle without a human operator. UAV related case study publications have been increased since last two decades. Detailed three-dimensional (3D) information on the land surface can be obtained from high spatial resolution point clouds. Modelling the terrain requires up-to date information. UAV can provide high-resolution images with low cost in the order of centimeters. We can reconstruct the terrain in a 3D representation using photogrammetry. In this study, we model a village located in Aksaray city using UAV photogrammetry. We created the orthomosaic and Digital Surface Map (DSM) of the region to characterize the terrain in detail. The obtained model and maps will help us to generate modern living space.

1. Introduction

Remote sensing plays a significant role in modelling the terrain and disaster management. Satellite, unmanned aerial vehicle (UAV) and LiDAR are the most used remote sensing techniques. Satellite image resolution is not sufficient for detection of small changes in land. LİDAR is an expensive technology. UAV, high resolution, is a practical tool for modelling the terrain. Three-dimensional (3D) visualization of the study area can be easily performed.

In order to create healthy settlement areas, we need to see the environment with high resolution and accuracy. Unmanned Aerial Vehicle (UAV) has been used frequently to solve engineering problems since last decade. UAV photogrammetry enables us to model the environment in digital media. Therefore, engineers can find modern solutions in a practical way. Traditional land surveying is a time-consuming and dangerous method in many environments. UAV is a valuable tool to get information from terrain. High resolution point cloud can be obtained using a low-cost UAV in a practical way.

The land management planning of a city shows its development [1] such as location of main and intermediate roads, parking areas, shopping centers, school areas and administrative buildings. Mapping the terrain to prepare settlement areas is very important in today's context.

UAV has been frequently used in terrain modelling, natural hazards modelling, agricultural studies, mining, civil engineering applications and cultural heritage documentation.

Volume calculation [2-3], tree detection [4], shoreline detection [5], cultural heritage modelling [6-7], landslide site mapping [8-9], rockfall site mapping [10], energy line detection [11], coastal cliff mapping [12], road distress studies [13] and urban mapping [14] have been implemented using UAV point clouds in recent years. Moreover, Lucieer et al. [15] have determined horizontal displacements of a landslide using two DEMS with UAV. Rossi et al. 2018 have determined the volume and extent of the landslide, and the displacement along slope by comparing DTMs obtained using UAV.

* **Corresponding Author**

*(hmuraty@gmail.com) ORCID ID 0000-0002-9725-5792
(nusretaktan@hotmail.com) ORCID ID 0000-0003-2582-9395
(acolak68@hotmail.com) ORCID ID 0000-0003-2582-9395
(aydinalptekin@mersin.edu.tr ORCID ID 0000-0002-5605-0758

Cite this article

Yılmaz, H. M., Aktan, N., Çolak, A., & Alptekin, A. (2022). Modelling Ozancık village (Aksaray) in computer environment using UAV photogrammetry. *Mersin Photogrammetry Journal, 4(1), 32-36*

2. UAV Technology

Photogrammetry is a branch of science that creates information about the object and its surrounding.

With the development of technology, it has become possible to obtain data from points that are not easy to reach. UAV provides new opportunities for mapping and monitoring of environment [15]. UAV is used to collect aerial photography. High resolution Digital Surface Map (DSM) and orthomosaic can be obtained in a short time. These products allow us to prepare land management strategies.

In general, there are three types of UAV which are rotary wing, fixed wing and VTOL. In this study, we used fixed wing rotary UAV. E-Bee (Figure 1) has been equipped with an optical camera, DSC-WX220_4.4_4896x3672 (RGB), and it has been used to perform photogrammetric data acquisition in an area. Technical specifications are given in Table 1.

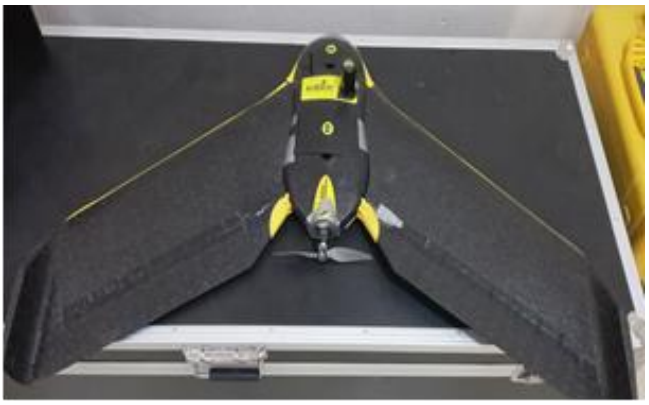

Figure 1. eBee SenseFly GZK UAV

Table 1. Technical specifications of EBee

Property	Value
Wingspan	116 cm
Weight	1.4 kg
Motor	Low-noise, brushless, electric
Radio link range	3 km nominal
Detachable wings	Yes
Camera options	senseFly S.O.D.A. 3D, senseFly Aeria X, senseFly Duet T, Parrot Sequoia+, senseFly S.O.D.A., senseFly Corridor, MicaSense RedEdge-MX
Flight & data management	eMotion
Cruise speed	40-110 km/h
Wind resistance	Up to 46 km/h
Max. flight time	59 minutes
Automatic landing	Yes
Landing type	Linear landing with Steep Landing technology
Ground Control Points (GCPs) required?	No, with included High-Precision on Demand (RTK/PPK)
Hand launched	Yes
Nominal coverage at 122 m	220 ha
Ground sampling distance at 122 m	2.5 cm/px
Absolute accuracy	Down to 3 cm

3. Study Area

In this study, we model Ozancık village located in Aksaray City, Turkey (Figure 2). The population of Ozancık village is decreasing each year. Ozancık village was founded in the 1700s.

Figure 2. Location map of the study area

UAV, E-Bee fixed wing, was used to obtain high quality pictures from field. UAV has taken 1227 pictures covering 3.97 km^2 area. Ground sampling Distance (GSD) was 4.24 cm.

Real time kinematics (RTK) is a surveying technique which can correct common errors in satellite navigation systems. RTK allows us not to use Ground Control Points (GCP). Relative position can be obtained with higher accuracy.

4. Modelling

In UAV photogrammetry, photographs of the region are taken with the flight plan prepared by taking into account the flight altitude, overlay ratio and flight speed parameters. The 3D model of the region is created by combining the pictures taken with the structure from motion method. Then DSM and orthophoto are produced.

Pictures taken from UAV has been imported into Pix4Dmapper software to adjustment, and ortomosaic (Figure 3a) and Digital Surface Map (Figure 3b) has been created. DSM, ortophoto and index details are shown in Table 2. Processing options are shown in Table 3. Error amounts after adjustment are shown in Table 4.

Pix4D mapper can transform aerial images to digital maps and 3D models. Mesh models, DSM, ortomosaic and index maps can be easily produced.

The high-resolution DSMs and orthophotos allowed the detection and the monitoring of fissures and small-scale changes of the surface.

DSM, geospatial feature, shows elevation values of environment. It includes both natural and artificial features.

Orthomosaic is a map that shows true location. It is a geometrically corrected map and represents Earth's surface.

Sfm can produce 3D model from 2D images using tie points. SfM method is cost-effective and practical tool.

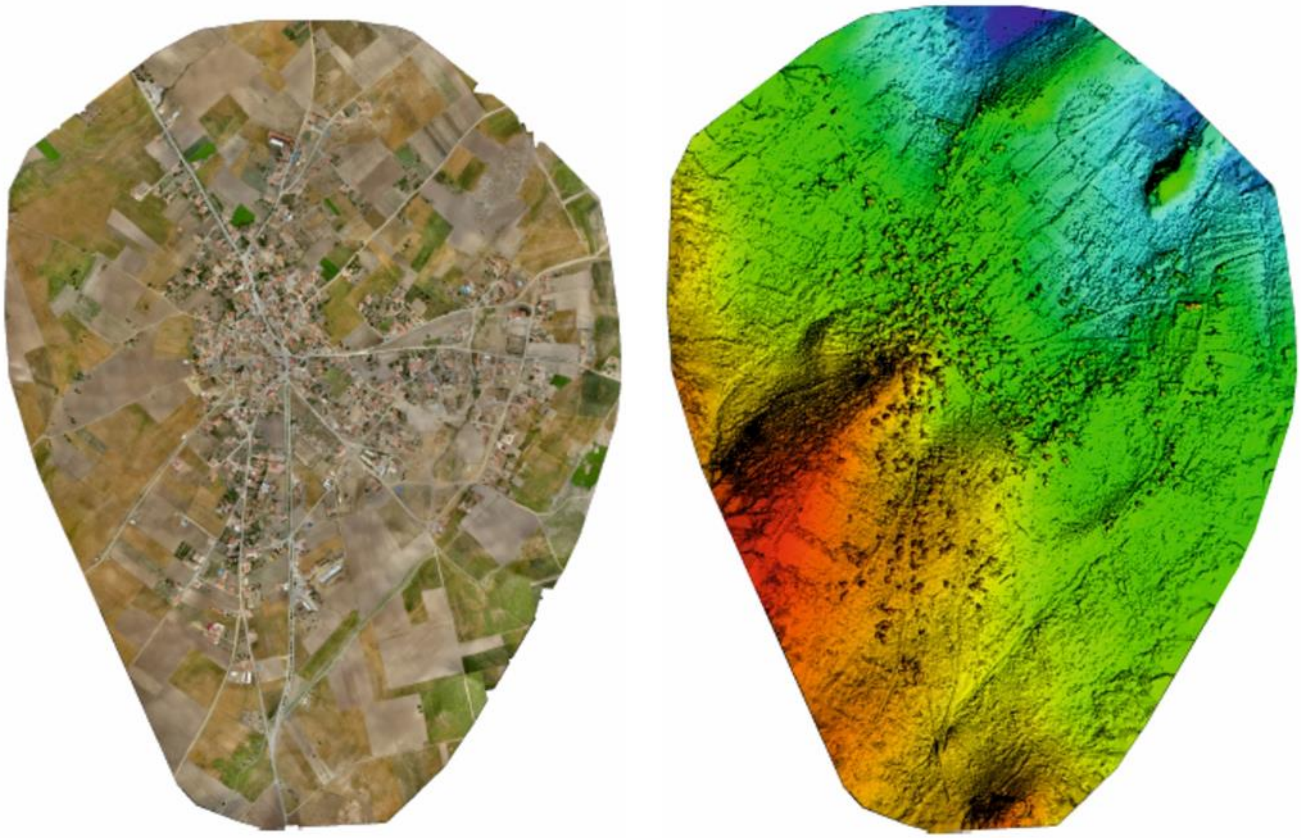

(a) (b)

Figure 3. Ortomosaic and DSM

Table 2. DSM, Orthomosaic and Index Details

DSM and Orthomosaic Resolution	1 x GSD (4.24 [cm/pixel])
DSM Filters	Noise Filtering: yes Surface Smoothing: yes, Type: Sharp
Raster DSM	Generated: yes Method: Inverse Distance Weighting Merge Tiles: yes
Orthomosaic	Generated: yes Merge Tiles: yes GeoTIFF Without Transparency: no Google Maps Tiles and KML: yes
Grid DSM	Generated: yes, Spacing [cm]: 100
Time for DSM Generation	01h:30m:41s
Time for Orthomosaic Generation	04h:11m:57s

Table 3. Processing options

Image Scale	multiscale, 1/2 (Half image size, Default)
Point Density	Optimal
Minimum Number of Matches	3
3D Textured Mesh Generation	yes
3D Textured Mesh Settings:	Resolution: Medium Resolution (default) Color Balancing: no
LOD	Generated: no
Advanced: 3D Textured Mesh Settings	Sample Density Divider: 1
Advanced: Image Groups	group1
Advanced: Use Processing Area	yes
Advanced: Use Annotations	yes
Time for Point Cloud Densification	03h:27m:02s
Time for 3D Textured Mesh Generation	40m:18s

Table 4. Error amounts

Mn Error [m]	Max Error [m]	Geolocation Error X [%]	Geolocation Error Y [%]	Geolocation Error Z [%]
-	-0.11	0.00	0.00	18.42
-0.11	-0.09	0.00	0.00	5.46
-0.09	-0.07	0.00	0.00	4.81
-0.07	-0.04	0.16	0.41	5.70
-0.04	-0.02	3.42	3.26	7.50
-0.02	0.00	46.62	44.50	6.36
0.00	0.02	45.88	47.19	6.76
0.02	0.04	3.75	3.99	7.25
0.04	0.07	0.16	0.65	5.87
0.07	0.09	0.00	0.00	6.03
0.09	0.11	0.00	0.00	6.19
0.11	-	0.00	0.00	19.64
Mean [m]		-0.000015	0.000581	-0.002184
Sigma [m]		0.012165	0.012794	0.128967
RMS Error [m]		0.012165	0.012807	0.128986

5. Discussion

There are some limitations in using UAV. Weather conditions, flight area and presence of high trees. Proper weather conditions play important role. Weather forecast has to be checked properly.

Although the spatial resolution of satellite imagery has significantly improved in the last decade, the data collected is still not sufficient for medium to small coastal changes (centimetric accuracy).

Environment management requires up to date information [12]. Small changes are not distinguishable at the spatial resolutions obtained using manned aircraft and satellite systems. We used Pix4D mapper because it automates the SfM pipeline in a user-friendly workflow.

Georeferenced orthophotos and DSM s are used to measure small changes.

Models can be used flow-direction studies, power line corridors and project managements.

UAV enables to produce maps in a short time. UAV offers the opportunity to fly close to the object [16].

Many villages are located in mountainous region. Mapping those terrain will not be possible sometimes. UAV will be very useful for those terrain.

6. Conclusion

In this study, products that can offer the opportunity to work in many professional disciplines have been produced. UAV photogrammetry helped us to map the terrain with high accuracy and resolution in an easy way. This research has demonstrated us successful mapping has been achieved. The obtained model and maps will help land management. These maps can be used as base maps for many engineering projects. This study has shown that all public institutions can easily obtain a model of the desired terrain with UAV photogrammetry.

Author contributions

Hacı Murat Yılmaz: Conceptualization, Methodology, Software **Nusret Aktan:** Data curation, Writing-Original draft preparation, Software, Validation. **Adem Çolak:** Visualization, Investigation. **Aydın Alptekin:** Writing-Reviewing and Editing

Conflicts of interest

The authors declare no conflicts of interest.

References

1. Kaya, E., & Güngör, M. (2021). Numerical data generation using unmanned aerial vehicle: a case study of Aksaray Güzelyurt District. *Advanced UAV*, *1*(1), 34-39.
2. Şahin, V. & Yılmaz, H. M. (2021). Hacim Hesaplarında İnsansız Hava Aracı (İHA) Verilerinin Kullanılabilirliğinin Araştırılması. Türkiye İnsansız Hava Araçları Dergisi, 3 (2), 36-48. DOI: 10.51534/tiha.955271
3. Alptekin, A., & Yakar, M. (2020). Determination of pond volume with using an unmanned aerial vehicle. Mersin Photogrammetry Journal, 2(2), 59-63.
4. Ceylan, M. C. & Uysal, M. (2021). İnsansız hava aracı ile elde edilen veriler yardımıyla ağaç çıkarımı. Türkiye Fotogrametri Dergisi, 3 (1), 15-21. DOI: 10.53030/tufod.912501
5. Ünel, F. B., Kuşak, L., Çelik, M., Alptekin, A., & Yakar, M. (2020). Kıyı çizgisinin belirlenerek mülkiyet durumunun incelenmesi. Türkiye Arazi Yönetimi Dergisi, 2(1), 33-40.

6. Alptekin, A., & Yakar, M. (2021). 3D model of Üçayak Ruins obtained from point clouds. *Mersin Photogrammetry Journal*, *3*(2), 37-40.
7. Kanun, E., Alptekin, A., & Yakar, M. (2021). Cultural heritage modelling using UAV photogrammetric methods: a case study of Kanlıdivane archeological site. Advanced UAV, 1(1), 24-33.
8. Alptekin, A., & Yakar, M. (2020). Heyelan bölgesinin İHA kullanarak modellenmesi. Türkiye İnsansız Hava Araçları Dergisi, 2(1), 17-21.
9. Zeybek, M., & Şanlıoğlu, İ. (2020). Investigation of landslide detection using radial basis functions: a case study of the Taşkent landslide, Turkey. Environmental monitoring and assessment, 192(4), 1-19.
10. Alptekin, A., Çelik, M. Ö., Doğan, Y., & Yakar, M. (2019). Mapping of a rockfall site with an unmanned aerial vehicle. Mersin Photogrammetry Journal, 1(1), 12-16.
11. Karabacak, A. (2021). İnsansız hava araçları (İHA) İle enerji nakil hatlarının ölçülmesi üzerine derleme. *Türkiye Fotogrametri Dergisi*, *3*(1), 1-8.
12. Papakonstantinou, A., Topouzelis, K., & Pavlogeorgatos, G. (2016). Coastline zones identification and 3D coastal mapping using UAV spatial data. ISPRS International Journal of Geo-Information, 5(6), 75.
13. Zeybek, M., & Biçici, S. (2020). Road distress measurements using UAV. Turkish Journal of Remote Sensing and GIS, 1(1), 13-23.
14. Zeybek, M. (2021). Classification of UAV point clouds by random forest machine learning algorithm. Turkish Journal of Engineering, 5(2), 48-57.
15. Lucieer, A., Jong, S. M. D., & Turner, D. (2014). Mapping landslide displacements using Structure from Motion (SfM) and image correlation of multi-temporal UAV photography. *Progress in physical geography*, *38*(1), 97-116.
16. Kabadayı, A. (2021). Unmanned aerial vehicle usage in rough areas and photogrammetric data generation. Advanced UAV, 1(1), 8-14.